Title

Observation and study of the baryonic B-meson decays B→D(*)pp¯(π)(π)

Journal

Physical Review D, 85(9)

ISSN

2470-0010

Authors

del Amo Sanchez, P
Lees, JP
Poireau, V
et al.

Publication Date

2012-05-01

DOI

10.1103/physrevd.85.092017

Observation and study of the baryonic B-meson decays $B \to D^{(*)} p\bar{p}(\pi)(\pi)$

P. del Amo Sanchez,[1] J. P. Lees,[1] V. Poireau,[1] E. Prencipe,[1] V. Tisserand,[1] J. Garra Tico,[2] E. Grauges,[2] M. Martinelli,[3a,3b] A. Palano,[3a,3b] M. Pappagallo,[3a,3b] G. Eigen,[4] B. Stugu,[4] L. Sun,[4] M. Battaglia,[5] D. N. Brown,[5] B. Hooberman,[5] L. T. Kerth,[5] Yu. G. Kolomensky,[5] G. Lynch,[5] I. L. Osipenkov,[5] T. Tanabe,[5] C. M. Hawkes,[6] A. T. Watson,[6] H. Koch,[7] T. Schroeder,[7] D. J. Asgeirsson,[8] C. Hearty,[8] T. S. Mattison,[8] J. A. McKenna,[8] A. Khan,[9] A. Randle-Conde,[9] V. E. Blinov,[10] A. R. Buzykaev,[10] V. P. Druzhinin,[10] V. B. Golubev,[10] A. P. Onuchin,[10] S. I. Serednyakov,[10] Yu. I. Skovpen,[10] E. P. Solodov,[10] K. Yu. Todyshev,[10] A. N. Yushkov,[10] M. Bondioli,[11] S. Curry,[11] D. Kirkby,[11] A. J. Lankford,[11] M. Mandelkern,[11] E. C. Martin,[11] D. P. Stoker,[11] H. Atmacan,[12] J. W. Gary,[12] F. Liu,[12] O. Long,[12] G. M. Vitug,[12] C. Campagnari,[13] J. M. Flanigan,[13] T. M. Hong,[13] D. Kovalskyi,[13] J. D. Richman,[13] C. West,[13] A. M. Eisner,[14] C. A. Heusch,[14] J. Kroseberg,[14] W. S. Lockman,[14] A. J. Martinez,[14] T. Schalk,[14] B. A. Schumm,[14] A. Seiden,[14] L. O. Winstrom,[14] C. H. Cheng,[15] D. A. Doll,[15] B. Echenard,[15] D. G. Hitlin,[15] P. Ongmongkolkul,[15] F. C. Porter,[15] A. Y. Rakitin,[15] R. Andreassen,[16] M. S. Dubrovin,[16] G. Mancinelli,[16] B. T. Meadows,[16] M. D. Sokoloff,[16] P. C. Bloom,[17] W. T. Ford,[17] A. Gaz,[17] M. Nagel,[17] U. Nauenberg,[17] J. G. Smith,[17] S. R. Wagner,[17] R. Ayad,[18,*] W. H. Toki,[18] H. Jasper,[19] T. M. Karbach,[19] J. Merkel,[19] A. Petzold,[19] B. Spaan,[19] K. Wacker,[19] M. J. Kobel,[20] K. R. Schubert,[20] R. Schwierz,[20] D. Bernard,[21] M. Verderi,[21] P. J. Clark,[22] S. Playfer,[22] J. E. Watson,[22] M. Andreotti,[23a,23b] D. Bettoni,[23a] C. Bozzi,[23a] R. Calabrese,[23a,23b] A. Cecchi,[23a,23b] G. Cibinetto,[23a,23b] E. Fioravanti,[23a,23b] P. Franchini,[23a,23b] E. Luppi,[23a,23b] M. Munerato,[23a,23b] M. Negrini,[23a,23b] A. Petrella,[23a,23b] L. Piemontese,[23a] R. Baldini-Ferroli,[24] A. Calcaterra,[24] R. de Sangro,[24] G. Finocchiaro,[24] M. Nicolaci,[24] S. Pacetti,[24] P. Patteri,[24] I. M. Peruzzi,[24,†] M. Piccolo,[24] M. Rama,[24] A. Zallo,[24] R. Contri,[25a,25b] E. Guido,[25a,25b] M. Lo Vetere,[25a,25b] M. R. Monge,[25a,25b] S. Passaggio,[25a] C. Patrignani,[25a,25b] E. Robutti,[25a] S. Tosi,[25a,25b] B. Bhuyan,[26] V. Prasad,[26] C. L. Lee,[27] M. Morii,[27] A. Adametz,[28] J. Marks,[28] U. Uwer,[28] F. U. Bernlochner,[29] M. Ebert,[29] H. M. Lacker,[29] T. Lueck,[29] A. Volk,[29] P. D. Dauncey,[30] M. Tibbetts,[30] P. K. Behera,[31] U. Mallik,[31] C. Chen,[32] J. Cochran,[32] H. B. Crawley,[32] L. Dong,[32] W. T. Meyer,[32] S. Prell,[32] E. I. Rosenberg,[32] A. E. Rubin,[32] A. V. Gritsan,[33] Z. J. Guo,[33] N. Arnaud,[34] M. Davier,[34] D. Derkach,[34] J. Firmino da Costa,[34] G. Grosdidier,[34] F. Le Diberder,[34] A. M. Lutz,[34] B. Malaescu,[34] A. Perez,[34] P. Roudeau,[34] M. H. Schune,[34] J. Serrano,[34] V. Sordini,[34,‡] A. Stocchi,[34] L. Wang,[34] G. Wormser,[34] D. J. Lange,[35] D. M. Wright,[35] I. Bingham,[36] C. A. Chavez,[36] J. P. Coleman,[36] J. R. Fry,[36] E. Gabathuler,[36] R. Gamet,[36] D. E. Hutchcroft,[36] D. J. Payne,[36] C. Touramanis,[36] A. J. Bevan,[37] F. Di Lodovico,[37] R. Sacco,[37] M. Sigamani,[37] G. Cowan,[38] S. Paramesvaran,[38] A. C. Wren,[38] D. N. Brown,[39] C. L. Davis,[39] A. G. Denig,[40] M. Fritsch,[40] W. Gradl,[40] A. Hafner,[40] K. E. Alwyn,[41] D. Bailey,[41] R. J. Barlow,[41] G. Jackson,[41] G. D. Lafferty,[41] J. Anderson,[42] R. Cenci,[42] A. Jawahery,[42] D. A. Roberts,[42] G. Simi,[42] J. M. Tuggle,[42] C. Dallapiccola,[43] E. Salvati,[43] R. Cowan,[44] D. Dujmic,[44] G. Sciolla,[44] M. Zhao,[44] D. Lindemann,[45] P. M. Patel,[45] S. H. Robertson,[45] M. Schram,[45] P. Biassoni,[46a,46b] A. Lazzaro,[46a,46b] V. Lombardo,[46a] F. Palombo,[46a,46b] S. Stracka,[46a,46b] L. Cremaldi,[47] R. Godang,[47,§] R. Kroeger,[47] P. Sonnek,[47] D. J. Summers,[47] X. Nguyen,[48] M. Simard,[48] P. Taras,[48] G. De Nardo,[49a,49b] D. Monorchio,[49a,49b] G. Onorato,[49a,49b] C. Sciacca,[49a,49b] G. Raven,[50] H. L. Snoek,[50] C. P. Jessop,[51] K. J. Knoepfel,[51] J. M. LoSecco,[51] W. F. Wang,[51] L. A. Corwin,[52] K. Honscheid,[52] R. Kass,[52] J. P. Morris,[52] N. L. Blount,[53] J. Brau,[53] R. Frey,[53] O. Igonkina,[53] J. A. Kolb,[53] R. Rahmat,[53] N. B. Sinev,[53] D. Strom,[53] J. Strube,[53] E. Torrence,[53] G. Castelli,[54a,54b] E. Feltresi,[54a,54b] N. Gagliardi,[54a,54b] M. Margoni,[54a,54b] M. Morandin,[54a] M. Posocco,[54a] M. Rotondo,[54a] F. Simonetto,[54a,54b] R. Stroili,[54a,54b] E. Ben-Haim,[55] G. R. Bonneaud,[55] H. Briand,[55] G. Calderini,[55] J. Chauveau,[55] O. Hamon,[55] Ph. Leruste,[55] G. Marchiori,[55] J. Ocariz,[55] J. Prendki,[55] S. Sitt,[55] M. Biasini,[56a,56b] E. Manoni,[56a,56b] A. Rossi,[56a,56b] C. Angelini,[57a,57b] G. Batignani,[57a,57b] S. Bettarini,[57a,57b] M. Carpinelli,[57a,57b,‖] G. Casarosa,[57a,57b] A. Cervelli,[57a,57b] F. Forti,[57a,57b] M. A. Giorgi,[57a,57b] A. Lusiani,[57a,57c] N. Neri,[57a,57b] E. Paoloni,[57a,57b] G. Rizzo,[57a,57b] J. J. Walsh,[57a] D. Lopes Pegna,[58] C. Lu,[58] J. Olsen,[58] A. J. S. Smith,[58] A. V. Telnov,[58] F. Anulli,[59a] E. Baracchini,[59a,59b] G. Cavoto,[59a] R. Faccini,[59a,59b] F. Ferrarotto,[59a] F. Ferroni,[59a,59b] M. Gaspero,[59a,59b] L. Li Gioi,[59a] M. A. Mazzoni,[59a] G. Piredda,[59a] F. Renga,[59a,59b] T. Hartmann,[60] T. Leddig,[60] H. Schröder,[60] R. Waldi,[60] T. Adye,[61] B. Franek,[61] E. O. Olaiya,[61] F. F. Wilson,[61] S. Emery,[62] G. Hamel de Monchenault,[62] G. Vasseur,[62] Ch. Yèche,[62] M. Zito,[62] M. T. Allen,[63] D. Aston,[63] D. J. Bard,[63] R. Bartoldus,[63] J. F. Benitez,[63] C. Cartaro,[63] M. R. Convery,[63] J. Dorfan,[63] G. P. Dubois-Felsmann,[63] W. Dunwoodie,[63] R. C. Field,[63] M. Franco Sevilla,[63] B. G. Fulsom,[63] A. M. Gabareen,[63] M. T. Graham,[63] P. Grenier,[63] C. Hast,[63] W. R. Innes,[63] M. H. Kelsey,[63] H. Kim,[63] P. Kim,[63] M. L. Kocian,[63] D. W. G. S. Leith,[63] S. Li,[63] B. Lindquist,[63] S. Luitz,[63] V. Luth,[63] H. L. Lynch,[63] D. B. MacFarlane,[63] H. Marsiske,[63] D. R. Muller,[63] H. Neal,[63] S. Nelson,[63] C. P. O'Grady,[63] I. Ofte,[63] M. Perl,[63] T. Pulliam,[63] B. N. Ratcliff,[63] A. Roodman,[63] A. A. Salnikov,[63] V. Santoro,[63] R. H. Schindler,[63] J. Schwiening,[63] A. Snyder,[63] D. Su,[63] M. K. Sullivan,[63] S. Sun,[63]

K. Suzuki,[63] J. M. Thompson,[63] J. Va'vra,[63] A. P. Wagner,[63] M. Weaver,[63] C. A. West,[63] W. J. Wisniewski,[63] M. Wittgen,[63] D. H. Wright,[63] H. W. Wulsin,[63] A. K. Yarritu,[63] C. C. Young,[63] V. Ziegler,[63] X. R. Chen,[64] W. Park,[64] M. V. Purohit,[64] R. M. White,[64] J. R. Wilson,[64] S. J. Sekula,[65] M. Bellis,[66] P. R. Burchat,[66] A. J. Edwards,[66] T. S. Miyashita,[66] S. Ahmed,[67] M. S. Alam,[67] J. A. Ernst,[67] B. Pan,[67] M. A. Saeed,[67] S. B. Zain,[67] N. Guttman,[68] A. Soffer,[68] P. Lund,[69] S. M. Spanier,[69] R. Eckmann,[70] J. L. Ritchie,[70] A. M. Ruland,[70] C. J. Schilling,[70] R. F. Schwitters,[70] B. C. Wray,[70] J. M. Izen,[71] X. C. Lou,[71] F. Bianchi,[72a,72b] D. Gamba,[72a,72b] M. Pelliccioni,[72a,72b] M. Bomben,[73a,73b] L. Lanceri,[73a,73b] L. Vitale,[73a,73b] N. Lopez-March,[74] F. Martinez-Vidal,[74] D. A. Milanes,[74] A. Oyanguren,[74] J. Albert,[75] Sw. Banerjee,[75] H. H. F. Choi,[75] K. Hamano,[75] G. J. King,[75] R. Kowalewski,[75] M. J. Lewczuk,[75] I. M. Nugent,[75] J. M. Roney,[75] R. J. Sobie,[75] T. J. Gershon,[76] P. F. Harrison,[76] T. E. Latham,[76] E. M. T. Puccio,[76] H. R. Band,[77] S. Dasu,[77] K. T. Flood,[77] Y. Pan,[77] R. Prepost,[77] C. O. Vuosalo,[77] and S. L. Wu[77]

(*BABAR* Collaboration)

[1]*Laboratoire d'Annecy-le-Vieux de Physique des Particules (LAPP), Université de Savoie, CNRS/IN2P3, F-74941 Annecy-Le-Vieux, France*
[2]*Universitat de Barcelona, Facultat de Fisica, Departament ECM, E-08028 Barcelona, Spain*
[3a]*INFN Sezione di Bari, I-70126 Bari, Italy*
[3b]*Dipartimento di Fisica, Università di Bari, I-70126 Bari, Italy*
[4]*University of Bergen, Institute of Physics, N-5007 Bergen, Norway*
[5]*Lawrence Berkeley National Laboratory and University of California, Berkeley, California 94720, USA*
[6]*University of Birmingham, Birmingham, B15 2TT, United Kingdom*
[7]*Ruhr Universität Bochum, Institut für Experimentalphysik 1, D-44780 Bochum, Germany*
[8]*University of British Columbia, Vancouver, British Columbia, Canada V6T 1Z1*
[9]*Brunel University, Uxbridge, Middlesex UB8 3PH, United Kingdom*
[10]*Budker Institute of Nuclear Physics, Novosibirsk 630090, Russia*
[11]*University of California at Irvine, Irvine, California 92697, USA*
[12]*University of California at Riverside, Riverside, California 92521, USA*
[13]*University of California at Santa Barbara, Santa Barbara, California 93106, USA*
[14]*University of California at Santa Cruz, Institute for Particle Physics, Santa Cruz, California 95064, USA*
[15]*California Institute of Technology, Pasadena, California 91125, USA*
[16]*University of Cincinnati, Cincinnati, Ohio 45221, USA*
[17]*University of Colorado, Boulder, Colorado 80309, USA*
[18]*Colorado State University, Fort Collins, Colorado 80523, USA*
[19]*Technische Universität Dortmund, Fakultät Physik, D-44221 Dortmund, Germany*
[20]*Technische Universität Dresden, Institut für Kern- und Teilchenphysik, D-01062 Dresden, Germany*
[21]*Laboratoire Leprince-Ringuet, CNRS/IN2P3, Ecole Polytechnique, F-91128 Palaiseau, France*
[22]*University of Edinburgh, Edinburgh EH9 3JZ, United Kingdom*
[23a]*INFN Sezione di Ferrara, I-44100 Ferrara, Italy*
[23b]*Dipartimento di Fisica, Università di Ferrara, I-44100 Ferrara, Italy*
[24]*INFN Laboratori Nazionali di Frascati, I-00044 Frascati, Italy*
[25a]*INFN Sezione di Genova, I-16146 Genova, Italy*
[25b]*Dipartimento di Fisica, Università di Genova, I-16146 Genova, Italy*
[26]*Indian Institute of Technology Guwahati, Guwahati, Assam, 781 039, India*
[27]*Harvard University, Cambridge, Massachusetts 02138, USA*
[28]*Universität Heidelberg, Physikalisches Institut, Philosophenweg 12, D-69120 Heidelberg, Germany*
[29]*Humboldt-Universität zu Berlin, Institut für Physik, Newtonstr. 15, D-12489 Berlin, Germany*
[30]*Imperial College London, London, SW7 2AZ, United Kingdom*
[31]*University of Iowa, Iowa City, Iowa 52242, USA*
[32]*Iowa State University, Ames, Iowa 50011-3160, USA*
[33]*Johns Hopkins University, Baltimore, Maryland 21218, USA*
[34]*Laboratoire de l'Accélérateur Linéaire, IN2P3/CNRS et Université Paris-Sud 11, Centre Scientifique d'Orsay, B. P. 34, F-91898 Orsay Cedex, France*
[35]*Lawrence Livermore National Laboratory, Livermore, California 94550, USA*
[36]*University of Liverpool, Liverpool L69 7ZE, United Kingdom*
[37]*Queen Mary, University of London, London, E1 4NS, United Kingdom*
[38]*University of London, Royal Holloway and Bedford New College, Egham, Surrey TW20 0EX, United Kingdom*
[39]*University of Louisville, Louisville, Kentucky 40292, USA*
[40]*Johannes Gutenberg-Universität Mainz, Institut für Kernphysik, D-55099 Mainz, Germany*

[41]*University of Manchester, Manchester M13 9PL, United Kingdom*
[42]*University of Maryland, College Park, Maryland 20742, USA*
[43]*University of Massachusetts, Amherst, Massachusetts 01003, USA*
[44]*Massachusetts Institute of Technology, Laboratory for Nuclear Science, Cambridge, Massachusetts 02139, USA*
[45]*McGill University, Montréal, Québec, Canada H3A 2T8*
[46a]*INFN Sezione di Milano, I-20133 Milano, Italy;*
[46b]*Dipartimento di Fisica, Università di Milano, I-20133 Milano, Italy*
[47]*University of Mississippi, University, Mississippi 38677, USA*
[48]*Université de Montréal, Physique des Particules, Montréal, Québec, Canada H3C 3J7*
[49a]*INFN Sezione di Napoli, I-80126 Napoli, Italy*
[49b]*Dipartimento di Scienze Fisiche, Università di Napoli Federico II, I-80126 Napoli, Italy*
[50]*NIKHEF, National Institute for Nuclear Physics and High Energy Physics, NL-1009 DB Amsterdam, The Netherlands*
[51]*University of Notre Dame, Notre Dame, Indiana 46556, USA*
[52]*Ohio State University, Columbus, Ohio 43210, USA*
[53]*University of Oregon, Eugene, Oregon 97403, USA*
[54a]*INFN Sezione di Padova, I-35131 Padova, Italy*
[54b]*Dipartimento di Fisica, Università di Padova, I-35131 Padova, Italy*
[55]*Laboratoire de Physique Nucléaire et de Hautes Energies, IN2P3/CNRS, Université Pierre et Marie Curie-Paris6, Université Denis Diderot-Paris7, F-75252 Paris, France*
[56a]*INFN Sezione di Perugia, I-06100 Perugia, Italy*
[56b]*Dipartimento di Fisica, Università di Perugia, I-06100 Perugia, Italy*
[57a]*INFN Sezione di Pisa, I-56127 Pisa, Italy*
[57b]*Dipartimento di Fisica, Università di Pisa, I-56127 Pisa, Italy*
[57c]*Scuola Normale Superiore di Pisa, I-56127 Pisa, Italy*
[58]*Princeton University, Princeton, New Jersey 08544, USA*
[59a]*INFN Sezione di Roma, I-00185 Roma, Italy*
[59b]*Dipartimento di Fisica, Università di Roma La Sapienza, I-00185 Roma, Italy*
[60]*Universität Rostock, D-18051 Rostock, Germany*
[61]*Rutherford Appleton Laboratory, Chilton, Didcot, Oxon, OX11 0QX, United Kingdom*
[62]*CEA, Irfu, SPP, Centre de Saclay, F-91191 Gif-sur-Yvette, France*
[63]*SLAC National Accelerator Laboratory, Stanford, California 94309 USA*
[64]*University of South Carolina, Columbia, South Carolina 29208, USA*
[65]*Southern Methodist University, Dallas, Texas 75275, USA*
[66]*Stanford University, Stanford, California 94305-4060, USA*
[67]*State University of New York, Albany, New York 12222, USA*
[68]*Tel Aviv University, School of Physics and Astronomy, Tel Aviv, 69978, Israel*
[69]*University of Tennessee, Knoxville, Tennessee 37996, USA*
[70]*University of Texas at Austin, Austin, Texas 78712, USA*
[71]*University of Texas at Dallas, Richardson, Texas 75083, USA*
[72a]*INFN Sezione di Torino, I-10125 Torino, Italy*
[72b]*Dipartimento di Fisica Sperimentale, Università di Torino, I-10125 Torino, Italy*
[73a]*INFN Sezione di Trieste, I-34127 Trieste, Italy*
[73b]*Dipartimento di Fisica, Università di Trieste, I-34127 Trieste, Italy*
[74]*IFIC, Universitat de Valencia-CSIC, E-46071 Valencia, Spain*
[75]*University of Victoria, Victoria, British Columbia, Canada V8W 3P6*
[76]*Department of Physics, University of Warwick, Coventry CV4 7AL, United Kingdom*
[77]*University of Wisconsin, Madison, Wisconsin 53706, USA*

(Received 21 November 2011; published 30 May 2012)

We present results for B-meson decay modes involving a charm meson, protons, and pions using 455×10^6 $B\bar{B}$ pairs recorded by the *BaBar* detector at the SLAC PEP-II asymmetric-energy e^+e^- collider. The branching fractions are measured for the following ten decays: $\bar{B}^0 \to D^0 p\bar{p}$, $\bar{B}^0 \to D^{*0} p\bar{p}$, $\bar{B}^0 \to D^+ p\bar{p}\pi^-$, $\bar{B}^0 \to D^{*+} p\bar{p}\pi^-$, $B^- \to D^0 p\bar{p}\pi^-$, $B^- \to D^{*0} p\bar{p}\pi^-$, $\bar{B}^0 \to D^0 p\bar{p}\pi^-\pi^+$, $\bar{B}^0 \to D^{*0} p\bar{p}\pi^-\pi^+$, $B^- \to D^+ p\bar{p}\pi^-\pi^-$, and $B^- \to D^{*+} p\bar{p}\pi^-\pi^-$. The four B^- and the two five-body $\bar{B}^0$

[*]Now at Temple University, Philadelphia, PA 19122, USA
[†]Also with Università di Perugia, Dipartimento di Fisica, Perugia, Italy
[‡]Also with Università di Roma La Sapienza, I-00185 Roma, Italy
[§]Now at University of South Alabama, Mobile, AL 36688, USA
[‖]Also with Università di Sassari, Sassari, Italy

modes are observed for the first time. The four-body modes are enhanced compared to the three- and the five-body modes. In the three-body modes, the $M(p\bar{p})$ and $M(D^{(*)0}p)$ invariant-mass distributions show enhancements near threshold values. In the four-body mode $\bar{B}^0 \to D^+ p\bar{p}\pi^-$, the $M(p\pi^-)$ distribution shows a narrow structure of unknown origin near 1.5 GeV/c^2. The distributions for the five-body modes, in contrast to the others, are similar to the expectations from uniform phase-space predictions.

DOI: 10.1103/PhysRevD.85.092017 PACS numbers: 13.25.Hw, 12.39.Mk, 14.20.Gk, 14.40.Nd

I. INTRODUCTION

B-meson decays to final states with baryons have been explored much less systematically than decays to meson-only final states. The first exclusively reconstructed decay modes were the CLEO observations of $B \to \Lambda_c^+ \bar{p}\pi$ and $B \to \Lambda_c^+ \bar{p}\pi\pi$ [1] and, later, of $\bar{B}^0 \to D^{*+} p\bar{p}\pi^-$ and $B^0 \to D^{*-} p\bar{n}$ [2]. These measurements supported the prediction [3] that the final states with Λ_c baryons are not the only sizable contributions to the baryonic B-meson decay rate, and that the charm-meson modes of the form $B \to D^{(*)} N\bar{N}' +$ anything, where the $N^{(\prime)}$ represent nucleon states, are also significant. Previous measurements show a trend that the branching fractions increase with the number of final-state particles. The branching fractions for the four-body modes $\bar{B}^0 \to D^{(*)+} p\bar{p}\pi^-$ [2,4] are approximately 4 times larger than those for the three-body modes $\bar{B}^0 \to D^{(*)0} p\bar{p}$ [5]. Furthermore, the branching fraction for the three-body mode $B^- \to \Lambda_c^+ \bar{p}\pi^-$ [6] is an order-of-magnitude larger than that for the two-body mode $\bar{B}^0 \to \Lambda_c^+ \bar{p}$ [7].

We expand the scope of baryonic B-decay studies with measurements of the branching fractions and the kinematic distributions of the following ten modes [8,9]: $\bar{B}^0 \to D^0 p\bar{p}$ and $\bar{B}^0 \to D^{*0} p\bar{p}$, $\bar{B}^0 \to D^+ p\bar{p}\pi^-$ and $\bar{B}^0 \to D^{*+} p\bar{p}\pi^-$, $B^- \to D^0 p\bar{p}\pi^-$ and $\bar{B}^0 \to D^{*0} p\bar{p}\pi^-$, $\bar{B}^0 \to D^0 p\bar{p}\pi^-\pi^+$ and $\bar{B}^0 \to D^{*0} p\bar{p}\pi^-\pi^+$, $B^- \to D^+ p\bar{p}\pi^-\pi^-$ and $B^- \to D^{*+} p\bar{p}\pi^-\pi^-$. Six of the modes—the four B^- and the two five-body B^0 modes—are observed for the first time.

We reconstruct the modes through 26 decay chains consisting of all-hadronic final states (the list is given later with the results in Table I), e.g.,

$$B^+ \to D^{*-} p\bar{p}\pi^+\pi^+ \\ \hookrightarrow \bar{D}^0\pi^- \\ \hookrightarrow K^+\pi^-\pi^+\pi^-.$$

A D^0 meson, as in the above example, is produced in eight of the B modes and a D^+ is produced in the remaining two. The D^0-meson candidates are reconstructed through decays to $K^-\pi^+$, $K^-\pi^+\pi^0$, and $K^-\pi^+\pi^-\pi^+$; and the D^+ to $K^-\pi^+\pi^+$. The D^{*0}-meson candidates are reconstructed through decays to $D^0\pi^0$ and the D^{*+} as $D^0\pi^+$.

Typical quarkline diagrams for the three- and four-body modes with a $D^{(*)0}$ meson are shown in Fig. 1. The three-body modes involve internal emissions of the W^- boson, whereas the four- and five-body modes involve internal and external emission diagrams.

Baryonic B decays have a distinctive phenomenology whose features contrast with the patterns observed in meson-only final states. Experimentally, the overall rate enhancement of multibody decays and the low-mass enhancement in the baryon-antibaryon subsystem are observed [10–15]. Theoretically, these modes are used to investigate a wide range of topics [16–26]. Among them are the predictions of the relative branching fractions, the decay dynamics, and the hypotheses involving exotic QCD phenomena, such as tetra-, penta-, or septa-quark bound states. In particular, there have been discussions of $p\bar{p}$ peaks near threshold values and penta-quark intermediate resonance decays $\Theta_c \to D^{(*)+}\bar{p}$ with respect to our modes [27–30].

The paper is organized as follows: Section II describes the data sample and the *BaBar* detector. Section III presents the analysis method, introducing the key variables $M_{\rm ES}$ and ΔE. Section IV shows the fits to the joint $M_{\rm ES}$-ΔE distributions. The fit yields and the corresponding branching fractions are given. Section V discusses the systematic uncertainties. Section VI presents the kinematic distributions. For the three-body modes, the Dalitz plots of $M^2(D^{(*)0}p)$ vs $M^2(p\bar{p})$ are given as well as the invariant mass plots of the variables. For the four- and five-body modes, the two-body subsystem invariant mass plots are given. In the four-body modes, we investigate a narrow structure in the $M(p\pi^-)$ distribution near 1.5 GeV/c^2. Section VII states the conclusions.

II. *BABAR* DETECTOR AND DATA SAMPLE

We use a data sample with integrated luminosity of 414 fb^{-1} (455×10^6 $B\bar{B}$) recorded at the center-of-mass energy $\sqrt{s} = 10.58$ GeV with the *BaBar* detector at the PEP-II e^+e^- collider. The e^+ and e^- beams circulate in the storage rings at momenta of 3.1 GeV/c and 9 GeV/c, respectively. The value of $\sqrt{s}$ corresponds to the $\Upsilon(4S)$ mass, maximizing the cross section for $e^+e^- \to b\bar{b} \to \Upsilon(4S) \to B\bar{B}$ events. The $B\bar{B}$ production accounts for approximately a quarter of the total hadronic cross section; the continuum processes $e^+e^- \to u\bar{u}$, $d\bar{d}$, $s\bar{s}$, and $c\bar{c}$ constitute the rest.

The main components of the *BaBar* detector [31] are the tracking system, the Detector of Internally-Reflected

TABLE I. Intermediate values for Table II: B-meson branching fractions for the decay chains. $N_{\rm sig}$ is the yield, $N_{\rm peak}$ is the measured contamination (item xvii in Table IV), and ϵ is the reconstruction efficiency. The uncertainties are statistical.

B modes, D modes	$N_{\rm sig} \pm \sigma_{\rm sig}$	$N_{\rm peak}$	ϵ (%)	$\mathcal{B} \pm \sigma_{\rm stat}$ (10^{-4})
$\bar{B}^0 \to D^0 p\bar{p}$, $K\pi$	351 ± 20	7.6	19.0	1.02 ± 0.06
$\bar{B}^0 \to D^0 p\bar{p}$, $K\pi\pi^0$	431 ± 28	24	7.0	0.95 ± 0.06
$\bar{B}^0 \to D^0 p\bar{p}$, $K\pi\pi\pi$	448 ± 27	10	9.9	1.21 ± 0.07
$\bar{B}^0 \to D^{*0} p\bar{p}$, $K\pi$	110 ± 12	−1.4	9.4	1.08 ± 0.12
$\bar{B}^0 \to D^{*0} p\bar{p}$, $K\pi\pi^0$	148 ± 15	3.9	3.2	1.17 ± 0.12
$\bar{B}^0 \to D^{*0} p\bar{p}$, $K\pi\pi\pi$	95 ± 14	5.5	5.2	0.76 ± 0.12
$\bar{B}^0 \to D^{+} p\bar{p}\pi^-$, $K\pi\pi$	1816 ± 53	55	12.6	3.32 ± 0.10
$\bar{B}^0 \to D^{*+} p\bar{p}\pi^-$, $K\pi$	392 ± 21	2.3	6.8	4.79 ± 0.26
$\bar{B}^0 \to D^{*+} p\bar{p}\pi^-$, $K\pi\pi^0$	601 ± 28	21	3.1	4.53 ± 0.22
$\bar{B}^0 \to D^{*+} p\bar{p}\pi^-$, $K\pi\pi\pi$	378 ± 22	20	3.7	3.92 ± 0.24
$B^- \to D^0 p\bar{p}\pi^-$, $K\pi$	1078 ± 38	13	15.9	3.79 ± 0.14
$B^- \to D^0 p\bar{p}\pi^-$, $K\pi\pi^0$	1176 ± 54	41	5.5	3.34 ± 0.16
$B^- \to D^0 p\bar{p}\pi^-$, $K\pi\pi\pi$	1296 ± 57	33	7.8	4.38 ± 0.20
$B^- \to D^{*0} p\bar{p}\pi^-$, $K\pi$	328 ± 22	2.1	7.7	3.86 ± 0.26
$B^- \to D^{*0} p\bar{p}\pi^-$, $K\pi\pi^0$	482 ± 35	47	2.9	3.99 ± 0.32
$B^- \to D^{*0} p\bar{p}\pi^-$, $K\pi\pi\pi$	343 ± 31	32	4.0	3.37 ± 0.34
$\bar{B}^0 \to D^0 p\bar{p}\pi^-\pi^+$, $K\pi$	438 ± 32	7.7	8.2	2.97 ± 0.22
$\bar{B}^0 \to D^0 p\bar{p}\pi^-\pi^+$, $K\pi\pi^0$	663 ± 65	160	2.9	2.83 ± 0.36[a]
$\bar{B}^0 \to D^0 p\bar{p}\pi^-\pi^+$, $K\pi\pi\pi$	770 ± 68	40	3.8	5.28 ± 0.48[a]
$\bar{B}^0 \to D^{*0} p\bar{p}\pi^-\pi^+$, $K\pi$	61 ± 12	1.8	2.9	1.87 ± 0.38
$\bar{B}^0 \to D^{*0} p\bar{p}\pi^-\pi^+$, $K\pi\pi^0$	142 ± 32	37	1.3	2.19 ± 0.66[a]
$\bar{B}^0 \to D^{*0} p\bar{p}\pi^-\pi^+$, $K\pi\pi\pi$	163 ± 30	13	1.3	4.93 ± 0.99[a]
$B^- \to D^+ p\bar{p}\pi^-\pi^-$, $K\pi\pi$	475 ± 37	6.6	6.7	1.66 ± 0.13
$B^- \to D^{*+} p\bar{p}\pi^-\pi^-$, $K\pi$	57 ± 9	−12	2.9	1.98 ± 0.26
$B^- \to D^{*+} p\bar{p}\pi^-\pi^-$, $K\pi\pi^0$	94 ± 14	−0.6	1.3	1.82 ± 0.27
$B^- \to D^{*+} p\bar{p}\pi^-\pi^-$, $K\pi\pi\pi$	66 ± 12	4.8	1.5	1.61 ± 0.32

[a]The rows marked by an ''a'' have large systematic uncertainties; see text. The charges of the pions are implied as well as the $D^{*0} \to D^0\pi^0$ and $D^{*+} \to D^0\pi^+$ decays, when applicable.

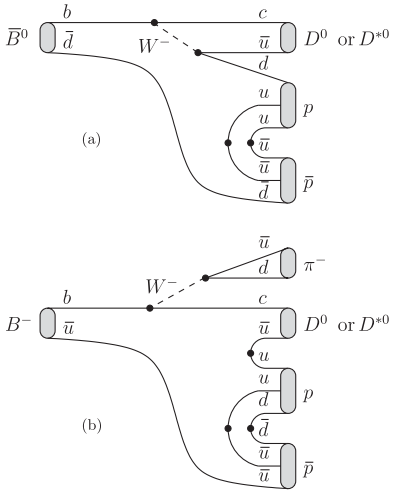

FIG. 1. Typical quarkline diagrams representing (a) $\bar{B}^0 \to D^{(*)0} p\bar{p}$ and (b) $B^- \to D^{(*)0} p\bar{p}\pi^-$ modes. The gluon lines are omitted.

Cherenkov radiation (DIRC), the electromagnetic calorimeter, and the instrumented flux return.

The two-part charged particle tracking system measures the momentum. The silicon vertex tracker, with five layers of double-sided silicon micro-strips, is closest to the interaction point. The tracker is followed by a wire drift chamber filled with a helium-isobutane (80:20) gas mixture, which was chosen to minimize multiple scattering. The superconducting coil creates a 1.5 T solenoidal field.

The DIRC measures the opening angle of the Cherenkov light cone, $\theta_{\rm C}$, produced by a charged particle traversing one of the 144 radiator bars of fused silica. The light propagates in the bar by total internal reflection and is projected onto an array of photomultiplier tubes surrounding a water-filled box mounted at the back end of the tracking system. The DIRC's ability to distinguish pions, kaons, and protons complements the energy loss measurements, dE/dx, in the tracking volume.

The calorimeter measures the energies and positions of electron-photon showers with an array of 6580 finely-segmented Tl-doped CsI crystals.

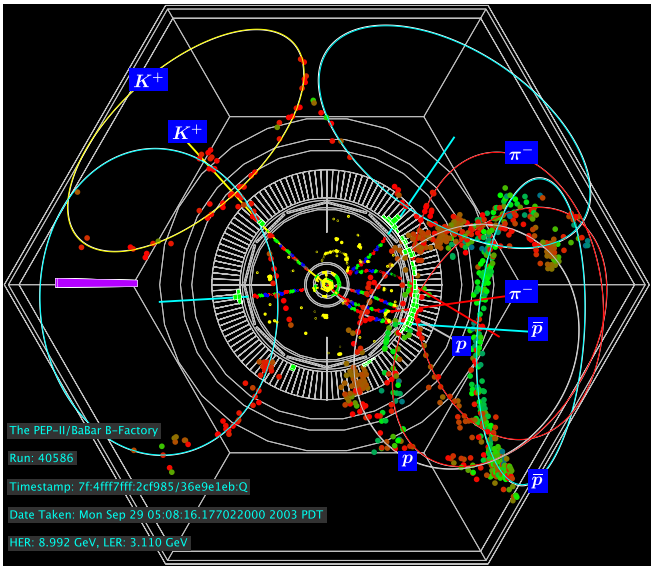

FIG. 2 (color online). Event display for the candidate decay $B^0 \to \bar{D}^0 p\bar{p}$, $\bar{D}^0 \to K^+\pi^-$. The labeled tracks in the tracking system and DIRC rings at the perimeter correspond to the particles in the reconstructed decay chain. The remaining unlabeled tracks and rings are due to the decay of the other $\bar{B}^0$ meson in the event. The beam axis is perpendicular to the image.

The flux return is instrumented with a combination of resistive plate chambers and limited streamer tubes for the detection of muons and neutral hadrons.

A data event display is given in Fig. 2 for the candidate decay $B^0 \to \bar{D}^0 p\bar{p}$, $\bar{D}^0 \to K^+\pi^-$.

III. ANALYSIS METHOD

This section describes the branching fraction measurement in four parts. Section III A describes the Monte Carlo-simulated event samples that are used to evaluate the performance of the method. Section III B lists the discriminating variables and their requirements for the event selection. Section III C defines the $M_{\rm ES}$ and ΔE variables and presents their distributions for the newly observed modes. Lastly, Sec. III D describes the fit to the $M_{\rm ES}$-ΔE distribution used to extract the signal yield.

A. Monte Carlo-simulated event samples

Monte Carlo (MC) event samples are produced and used to evaluate the analysis method. Two types of samples—signal and generic—are described below.

The particle decays are generated using a combination of EVTGEN [32] and JETSET 7.4 [33]. The interactions of the decay products traversing the detector are modeled by GEANT 4 [34]. The simulation takes into account varying detector conditions and beam backgrounds during the data-taking periods.

The signal MC sample is generated to characterize events with a B meson that decays to one of the signal modes (the accompanying $\bar{B}$ decays generically). The typical size of 3×10^5 events per decay chain is 2 orders of magnitude larger than the expected signal in data.

The generic MC sample is generated to characterize the entire data sample. The size is approximately twice that of the *BaBar* data sample.

B. Event selection

The e^+e^- events are filtered for a signal B-meson candidate through the pre- and the final selections.

The preselection requires the presence of proton-antiproton pair and a D^0- or a D^+-meson candidate (written as D without a charge designation) in one of the 26 decay chains listed in Sec. I.

Protons are identified with a likelihood-based algorithm using the dE/dx and the $\theta_{\rm C}$ measurements as described in Sec. II. For a 1.0 GeV/c proton in the lab frame (typical of those produced in a signal mode), the selection efficiency is 98% and the kaon fake rate is 1%.

The D-meson candidates are selected using the invariant mass [35], $M(D)$, and a kaon identification algorithm similar to that used for protons. The $M(D)$ is required to be within 7 times its resolution around the PDG value [6] (superseded later during final selection). For a 0.9 GeV/c kaon in the lab frame (typical of those produced in a signal mode), the selection efficiency is 85% and the pion fake rate is 2%.

For the $D^0 \to K^-\pi^+\pi^0$ and $D^{*0} \to D^0\pi^0$ subdecay modes, the $\pi^0 \to \gamma\gamma$ candidates are formed from two well-separated photons with $115 < M(\gamma\gamma) < 150$ MeV/c^2 or from two unseparated photons by using the second moment of the overlapping calorimeter energy deposits.

The charged particles from the decay chain are required to have a distance of closest approach to the beam spot of less than 1.5 cm.

The final selection requires the presence of a fully reconstructed signal B-meson candidate. Requirements on the discriminating variables described below are optimized by maximizing the signal precision $z = S/\sqrt{S+B}$, where S is the expected signal yield using the signal MC sample and B the expected background yield using the generic MC sample. The signal is normalized using the measured branching fractions for the modes $\bar{B}^0 \to D^{(*)0} p\bar{p}$ and $\bar{B}^0 \to D^{*+} p\bar{p}\pi^-$ [2,5]; for the rest of the modes the latter value is used. The quantity z is computed for each discriminating variable for each decay chain. For the variables with a broad maximum in z, the cut values are chosen to be consistent across similar modes.

In order to select D-meson candidates, $M(D)$ is required to be within $3\sigma_{M(D)}$ of the PDG value [6]. The resolutions $\sigma_{M(D)}$ for $D^0 \to K^-\pi^+$, $K^-\pi^+\pi^0$, $K^-\pi^+\pi^-\pi^+$, and $D^+ \to K^-\pi^+\pi^+$ are approximately 6, 10, 5, and 5 MeV/c^2, respectively. For the modes involving $D^0 \to K^-\pi^+\pi^0$ decays, the combinatoric background events due

to fake π^0 candidates are suppressed using a model [36] that parameterizes the amplitude of the Dalitz plot distribution $M^2(K^-\pi^+)$ vs $M^2(\pi^+\pi^0)$. The model accounts for the amplitudes and the interferences of decays of $K^{*0} \to K^-\pi^+$, $K^{*-} \to K^-\pi^0$, and $\rho^+ \to \pi^+\pi^0$. The normalized magnitude of the decay amplitude is used to suppress the background events by requiring the quantity to be greater than a value ranging from 1% to 5%, depending on the mode.

In order to select D^*-meson candidates, the D^*-D mass difference, $\Delta M = M(D^0\pi) - M(D^0)$, is required to be within $3\sigma_{\Delta M}$ of the PDG value [6]. The resolution $\sigma_{\Delta M}$ is approximately 0.8 MeV/c^2 for both $D^{*0} \to D^0\pi^0$ and $D^{*+} \to D^0\pi^+$. For the mode $\bar{B}^0 \to D^0 p\bar{p}\pi^-\pi^+$, the requirement of $\Delta M > 160$ MeV/c^2 excludes the contamination from $\bar{B}^0 \to D^{*+} p\bar{p}\pi^-$, $D^{*+} \to D^0\pi^+$ decays.

In order to select B-meson candidates, a combination of daughter particles in one of the signal modes is considered. The momentum vectors of the decay products are fit [37] while constraining $M(D)$ to the PDG value [6]. The vertex fit χ^2 probability for non-B events peaks sharply at zero; these events are suppressed by requiring the probability to be greater than 0.1%.

Continuum backgrounds events are suppressed by using the angle θ_{thrust} between the thrust axes [38] of the particles from the B-meson candidate and from the rest of the event. The continuum event distribution of $|\cos\theta_{\text{thrust}}|$ peaks at unity while it is uniform for $B\bar{B}$ events, so the quantity is required to be less than a value ranging from 0.8 to 1, depending on the mode.

After the selection, an average of 1.0 to 1.7 candidates per event remains for each decay chain and is largest for those decay chains with the largest particle multiplicity. If more than one candidate is present, we choose the one with the smallest value of

$$\delta = \frac{(M(D) - M(D)_{\text{PDG}})^2}{(\sigma_{M(D)})^2} + \frac{(\Delta M - \Delta M_{\text{PDG}})^2}{(\sigma_{\Delta M})^2}, \quad (1)$$

where the PDG values [6] are labeled as such. The latter term in the sum is included only if a D^* is present in the decay chain. If more than one candidate has the same δ value, we choose one randomly.

C. Definitions of M_{ES} and ΔE

The B meson beam-energy-substituted mass, M_{ES}, and the difference between its energy and the beam energy, ΔE, are defined with the quantities in the lab frame:

$$M_{\text{ES}} = \sqrt{\frac{(s + 4\boldsymbol{P}_B \cdot \boldsymbol{P}_0)^2}{4(E_0)^2} - (\boldsymbol{P}_B)^2}$$
$$\Delta E = \frac{Q_B \cdot Q_0}{\sqrt{s}} - \frac{\sqrt{s}}{2}. \quad (2)$$

The four-momentum vectors $Q_B = (E_B, \boldsymbol{P}_B)$ and $Q_0 = (E_0, \boldsymbol{P}_0)$ represent the B-meson candidate and the e^+e^- system, respectively. The two variables, when expressed in terms of center-of-mass quantities (denoted by asterisks), take the more familiar form, $M_{\text{ES}} = \sqrt{s/4 - (\boldsymbol{P}_B^*)^2}$ and $\Delta E = E_B^* - \sqrt{s}/2$.

The M_{ES}-ΔE distributions for the events passing the final selection are given for the six newly observed modes in Fig. 3. Each point represents a candidate in an event. For many of the modes, a dense concentration of events is visible near $M_{\text{ES}} = 5.28$ GeV/c^2, the PDG B-meson mass [6], and $\Delta E = 0$, as expected for signal events. The uniform distribution of events over the entire plane away from the signal area is indicative of the general smoothness of the background event distribution.

The M_{ES}-ΔE plots are given in a box region of $5.22 < M_{\text{ES}} < 5.30$ GeV/c^2 and $|\Delta E| < 50$ MeV. This box is large enough to provide a sufficient sideband region for each variable where no signal events reside. It is also small enough to exclude possible contamination from other similarly related B-meson decay modes.

For the purpose of plotting M_{ES} and ΔE individually, the box region is divided into a signal and a sideband region. The M_{ES} signal region is within $2.5\sigma_{M_{\text{ES}}}$ of the mean value of the Gaussian function describing it and likewise for ΔE. Similarly, the M_{ES} sideband region is outside $4\sigma_{M_{\text{ES}}}$ of the mean value and likewise for ΔE. The resolutions range from 2.2 to 2.5 MeV/c^2 for $\sigma_{M_{\text{ES}}}$ and 8 to 10 MeV/c^2 for $\sigma_{\Delta E}$. The signal box is the intersection of the M_{ES} and the ΔE signal regions.

D. Fit procedure

The signal yield is obtained by fitting the joint M_{ES}-ΔE distribution using a fit function in the framework of the extended maximum likelihood technique [39]. The likelihood value for N observed events,

$$L(\hat{N}, \hat{\Omega}) = \frac{e^{-\hat{N}}}{N!} \prod_{i=1}^{N} P(y_i; \hat{N}, \hat{\Omega}), \quad (3)$$

is a function of the yield estimate $\hat{N}$ and the set of parameters $\hat{\Omega}$. The y_i is the pair of M_{ES} and ΔE values for the B-meson candidate in the ith event and P is described below. The quantity L is maximized [40–42] with respect to its arguments.

The fit function is the sum of two terms

$$P(y_i; \hat{N}, \hat{\Omega}) = N_{\text{sig}} P_{\text{sig}}(y_i; \Omega_{\text{sig}}) + N_{\text{bgd}} P_{\text{bgd}}(y_i; \Omega_{\text{bgd}}), \quad (4)$$

which correspond to the signal and the background component, respectively. For each component function, P_α is the two-dimensional function, N_α the yield, and Ω_α the parameters. The arguments of the function components are related to the quantities in Eq. (4) by $\hat{N} = \sum_\beta N_\beta$ and $\hat{\Omega} = \bigcup_\beta \Omega_\beta$.

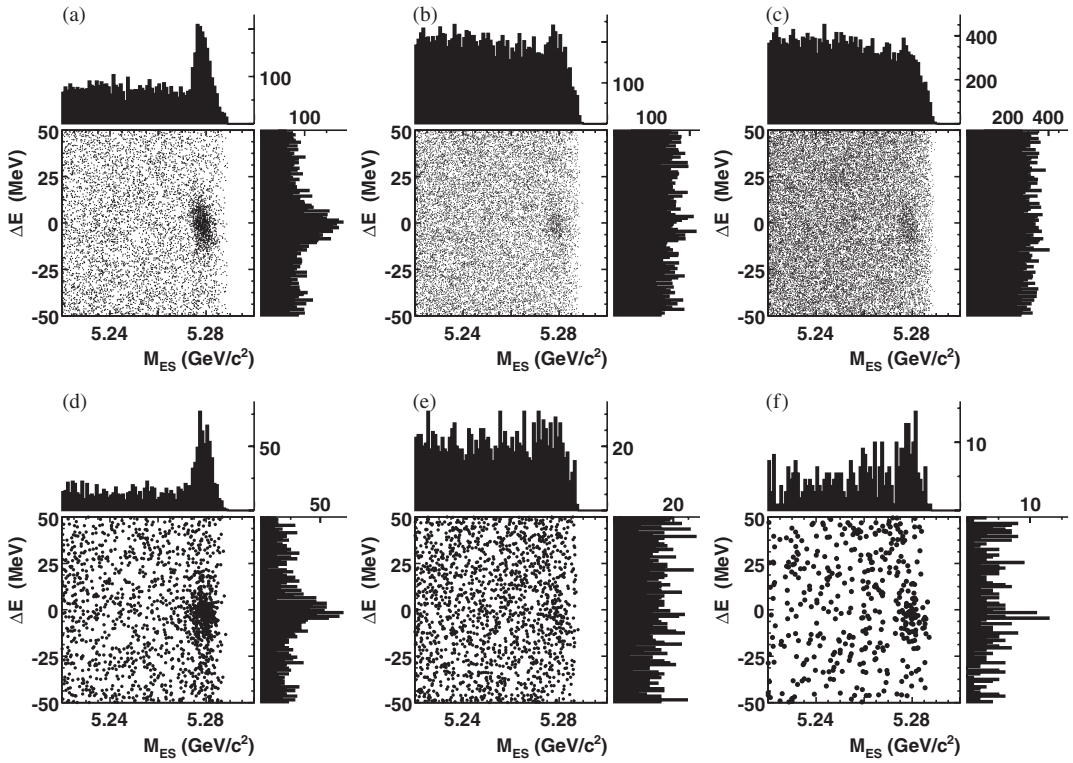

FIG. 3. Scatter plots of $M_{\rm ES} - \Delta E$ for the six newly observed B-meson decay modes: (a) $B^- \to D^0 p\bar{p}\pi^-$, (b) $\bar{B}^0 \to D^0 p\bar{p}\pi^-\pi^+$, (c) $B^- \to D^+ p\bar{p}\pi^-\pi^-$, (d) $B^- \to D^{*0} p\bar{p}\pi^-$, (e) $\bar{B}^0 \to D^{*0} p\bar{p}\pi^-\pi^+$, and (f) $B^- \to D^{*+} p\bar{p}\pi^-\pi^-$. The first row of plots is related to the second by the exchange of the charm meson $D \leftrightarrow D^*$. The decay chain involving $D^0 \to K^-\pi^+$ or $D^+ \to K^-\pi^+\pi^+$ is shown. For (d, e, f), the decay chain involves $D^{*0} \to D^0\pi^0$ or $D^{*+} \to D^0\pi^+$. The $M_{\rm ES}$ projection, in 1 MeV$/c^2$ bins, is given above the scatter plot; the ΔE, in 1 MeV bins, on the right. For the projection plots, no selection is made on the complementary variable.

Each function component P_α is written as the product of functions in $M_{\rm ES}$ and ΔE since the variables are largely uncorrelated. (The signal bias due to the small correlation is treated as a systematic uncertainty.) The distributions for signal events peak in each variable, so $P_{\rm sig}$ is the product of functions composed of a Gaussian core and a power-law tail [43]. The background event distribution varies smoothly, so $P_{\rm bgd}$ is the product of a threshold function [38] for $M_{\rm ES}$ that vanishes at approximately 5.29 GeV$/c^2$ and a second-order Chebyshev polynomial for ΔE.

The following function parameters are fixed to the values found by fitting the signal MC distributions: the ΔE Gaussian width for $P_{\rm sig}$, the $M_{\rm ES}$ Gaussian width for $P_{\rm sig}$, the $M_{\rm ES}$ power-law tail parameters for $P_{\rm sig}$, and the $M_{\rm ES}$ end-point parameter for $P_{\rm bgd}$. Two exceptions are given after the detailed fit example.

A detailed example of the fit results is given in Fig. 4 for the decay chain $B^- \to D^+ p\bar{p}\pi^-\pi^-$, $D^+ \to K^-\pi^+\pi^+$. The plots in Figs. 4(a) and 4(b) show the $M_{\rm ES}$ distributions for the ΔE signal and the ΔE sideband region, respectively. Likewise, Figs. 4(c) and 4(d)show the respective ΔE distributions for the analogous $M_{\rm ES}$ regions. The fit function projections describe the distributions in the sideband regions well [Figs. 4(b) and 4(d)], which gives us confidence that the background event distribution inside the signal box are also modeled well.

The first exception to the fit procedure described above applies to the mode $B^- \to D^{*0} p\bar{p}\pi^-$. A term is added to Eq. (4) to account for the sizable contamination from the mode $\bar{B}^0 \to D^{*+} p\bar{p}\pi^-$. The fit function $P_{\rm peak}$ is the same form as $P_{\rm sig}$ with its parameters fixed to the values found by fitting the MC sample. The normalization $N_{\rm peak}$ is based on the branching fraction measured in this paper.

The second exception applies to four decay chains whose fits do not converge: $\bar{B}^0 \to D^0 p\bar{p}\pi^-\pi^+$, $D^0 \to K^-\pi^+\pi^0$; $\bar{B}^0 \to D^0 p\bar{p}\pi^-\pi^+$, $D^0 \to K^-\pi^+\pi^-\pi^+$; $\bar{B}^0 \to D^{*0} p\bar{p}\pi^-\pi^+$, $D^{*0} \to D^0\pi^0$, $D^0 \to K^-\pi^+\pi^0$; and $\bar{B}^0 \to D^{*0} p\bar{p}\pi^-\pi^+$, $D^{*0} \to D^0\pi^0$, $D^0 \to K^-\pi^+\pi^-\pi^+$. Two changes are made: the Gaussian parameters are fixed to the values found in the $D^0 \to K^-\pi^+$ measurement, and the $M_{\rm ES}$ endpoint parameter is floated. The fits converge after the changes.

IV. BRANCHING FRACTIONS

This section presents the B-meson branching fractions $\mathcal{B}$. Section IV A shows the fits to the $M_{\rm ES}$-ΔE distributions. Sections IV B and IV C give the $\mathcal{B}$ values and their ratios, respectively. Throughout this section, we simply state and use the systematic uncertainties of Sec. V.

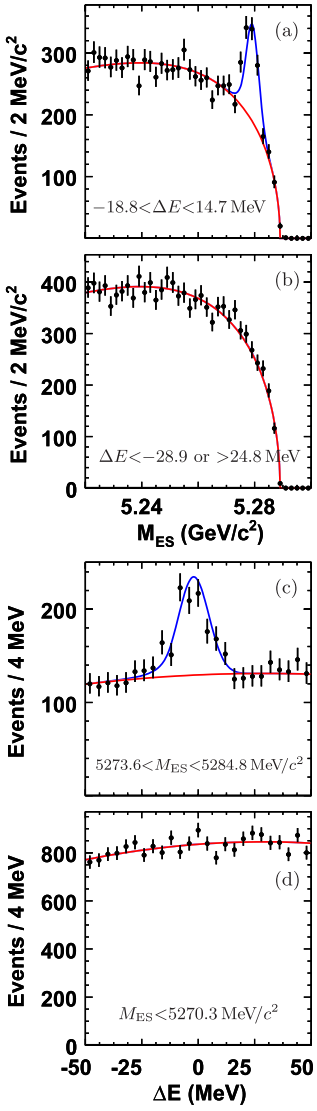

FIG. 4 (color online). Fit details for $B^- \to D^+ p\bar{p}\pi^-\pi^-$, $D^+ \to K^-\pi^+\pi^+$: $M_{\rm ES}$ and ΔE distributions in regions as noted on the plots. For (a, c) the top curve is the sum of $P_{\rm sig}$ and $P_{\rm bgd}$ and the bottom curve is the latter; for (b, d) the curve is $P_{\rm bgd}$.

A. Fits of $M_{\rm ES}$-ΔE distributions

The $M_{\rm ES}$ distributions for the events in the ΔE signal region for three-, four-, and five-body modes are given in Figs. 5–7, respectively. For all B-meson decay modes, the decay chains involving $D^0 \to K^-\pi^+$ or $D^+ \to K^-\pi^+\pi^+$ show a peak.

The fit function projection in each plot describes the data well, except for the four decay chains corresponding to Figs. 7(b)–7(d) and 7(f), which had difficulties with fit convergence as noted in the previous section. As we will see in Sec. V, the yields from these decay chains do not contribute significantly to the B-meson branching fraction, which is dominated by the value from $D^0 \to K^-\pi^+$, because of their relatively large systematic uncertainties.

The signal yields, given in Table I, range from 50 to 3500 events per mode.

B. Branching-fraction calculation

The B-meson branching fraction for each of the 26 decay chains, given in Table I, is given by

$$\mathcal{B} = \frac{1}{2N_{B\bar{B}}}\frac{1}{\mathcal{B}_\Upsilon \mathcal{B}_D \mathcal{B}_{D^*}}\frac{1}{\epsilon}(N_{\rm sig} - N_{\rm peak}), \qquad (5)$$

whose ingredients are as follows: the number of $B\bar{B}$ pairs, $N_{B\bar{B}} = 455 \times 10^6$, the assumed $\Upsilon(4S) \to B\bar{B}^0$ or $\to B^+B^-$ branching fraction, $\mathcal{B}_\Upsilon = 1/2$; the D-meson branching fraction, $\mathcal{B}_D$ [6]; the D^*-meson branching fraction, $\mathcal{B}_{D^*}$ [6]; the reconstruction efficiency, ϵ; the signal yield, $N_{\rm sig}$; and the measured contamination, $N_{\rm peak}$, using the $M(D)$-sideband data sample. The $\mathcal{B}_{D^*}$ is included only when a D^* decay is present in the decay chain. The efficiency ϵ is determined using the signal MC sample and decreases with the particle multiplicity. The mode $\bar{B}^0 \to D^0 p\bar{p}$, $D^0 \to K^-\pi^+$ has the highest value of ϵ at 19% and $\bar{B}^0 \to D^{*0} p\bar{p}\pi^-\pi^+$, $D^{*0} \to D^0\pi^0$ and $D^0 \to K^-\pi^+\pi^-\pi^+$ has the lowest at 1%.

The $\mathcal{B}$ values, given in Table II, are the combinations [44] of the above measurements using the statistical and the systematic uncertainties. All $\mathcal{B}$ values are significant with respect to their uncertainties. For the previously observed modes, the results are consistent with earlier measurements.

C. Branching-fraction ratios

Table III gives the ratio of the branching fractions $\mathcal{B}$ for modes related by $D \leftrightarrow D^*$, $D^{(*)0} \leftrightarrow D^{(*)+}$, and the addition of π. These ratios show four patterns:

(i) The ratios are roughly unity for the modes related by the spin of the charm mesons, $D \leftrightarrow D^*$. This result suggests that the additional degrees of freedom due to the D^* polarization vector do not significantly modify the production rate.
(ii) The ratio is roughly unity for the modes related by the charge of the charm mesons, $D^{(*)+} \leftrightarrow D^{(*)0}$,
(iii) The ratio for the four-body mode to that of the corresponding three-body mode with one fewer pion is about four.
(iv) The ratio for the five-body mode to that of the corresponding four-body mode with one fewer pion is about one-half.

The patterns (iii, iv) imply $\mathcal{B}_{\text{3-body}} < \mathcal{B}_{\text{5-body}} < \mathcal{B}_{\text{4-body}}$.

V. SYSTEMATIC UNCERTAINTIES

This section describes the systematic uncertainties for the B-meson branching fraction measurement. Section V A lists the sources, and Sec. V B gives the error matrices.

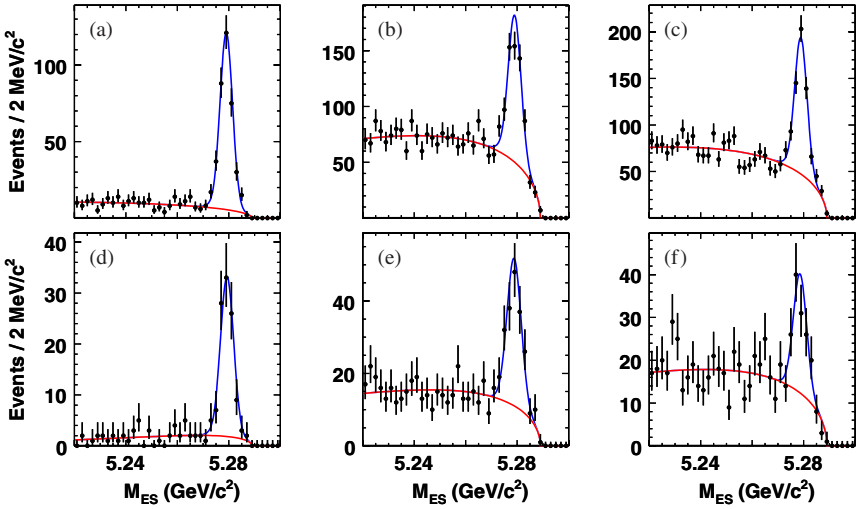

FIG. 5 (color online). $M_{\rm ES}$ fit projections for the three-body modes: (a–c) $\bar{B}^0 \to D^0 p\bar{p}$ and (d–f) $\bar{B}^0 \to D^{*0} p\bar{p}$, where (a, d) are reconstructed via $D^0 \to K^-\pi^+$, (b, e) $D^0 \to K^-\pi^+\pi^0$, and (c, f) $D^0 \to K^-\pi^+\pi^-\pi^+$; and (d–f) $D^{*0} \to D^0\pi^0$. Events with ΔE within 2.5σ of the mean value of the Gaussian function are shown. The top curve is the sum of $P_{\rm sig}$ and $P_{\rm bgd}$ and the bottom curve is the latter.

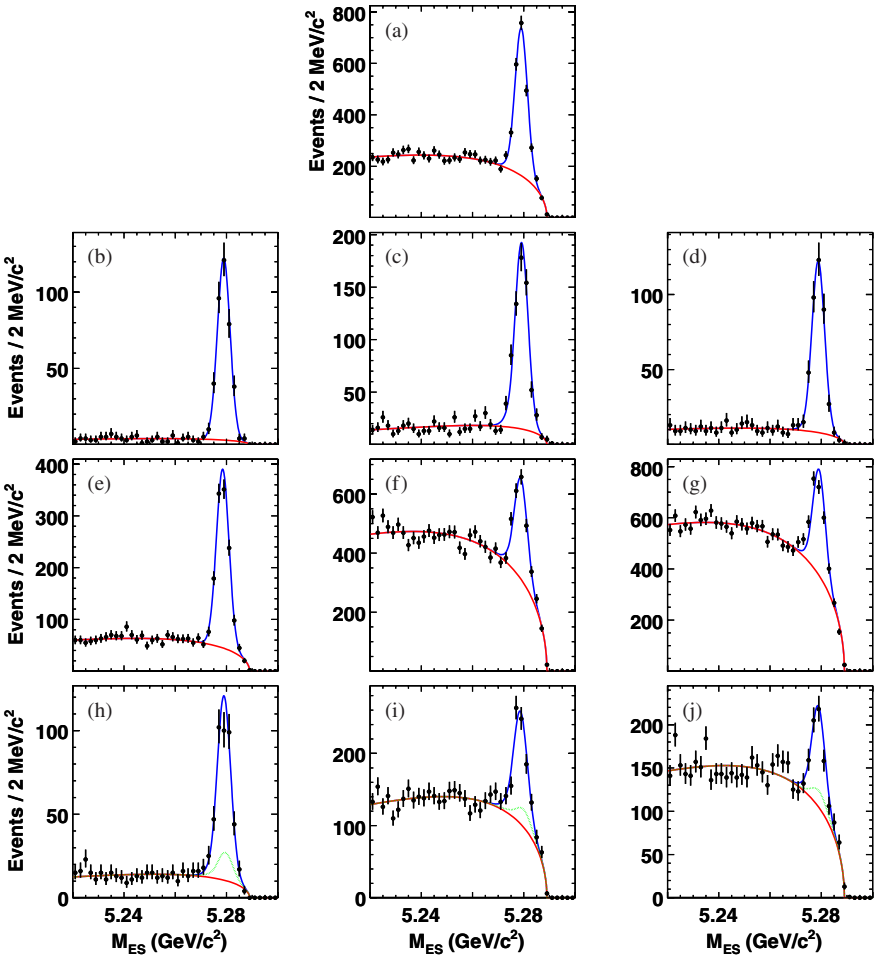

FIG. 6 (color online). $M_{\rm ES}$ fit projections for the four-body modes: (a) $\bar{B}^0 \to D^+ p\bar{p}\pi^-$, (b–d) $\bar{B}^0 \to D^{*+} p\bar{p}\pi^-$, (e–g) $B^- \to D^0 p\bar{p}\pi^-$, and (h–j) $B^- \to D^{*0} p\bar{p}\pi^-$, where (a) is reconstructed via $D^+ \to K^-\pi^+\pi^+$, (b, e, h) $D^0 \to K^-\pi^+$, (c, f, i) $D^0 \to K^-\pi^+\pi^0$, and (d, g, j) $D^0 \to K^-\pi^+\pi^-\pi^+$; and (b–d) $D^{*+} \to D^0\pi^+$ and (h–j) $D^{*0} \to D^0\pi^0$. Events with ΔE within 2.5σ of the Gaussian mean value are shown. For (a–g) the top curve is the sum of $P_{\rm sig}$ and $P_{\rm bgd}$ and the bottom curve is the latter; for (h–j) the middle curve is the sum of $P_{\rm peak}$ and $P_{\rm bgd}$.

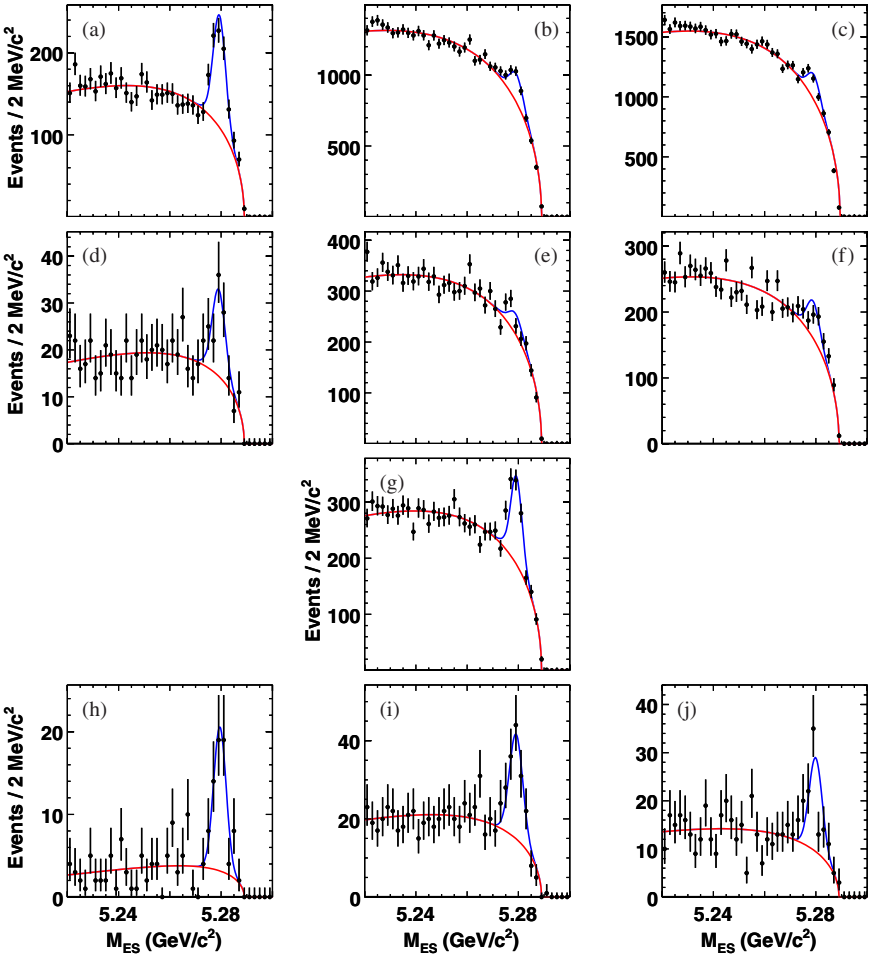

FIG. 7 (color online). $M_{\rm ES}$ fit projections for the five-body modes: (a–c) $\bar{B}^0 \to D^0 p\bar{p}\pi^-\pi^+$, (d–f) $\bar{B}^0 \to D^{*0} p\bar{p}\pi^-\pi^+$, (g) $B^- \to D^+ p\bar{p}\pi^-\pi^-$, and (h–j) $B^- \to D^{*+} p\bar{p}\pi^-\pi^-$, where (a, d, h) are reconstructed via $D^0 \to K^-\pi^+$, (b, e, i) $D^0 \to K^-\pi^+\pi^0$, (c, f, j) $D^0 \to K^-\pi^+\pi^-\pi^+$, and (g) $D^+ \to K^-\pi^+\pi^+$; and (b–d) $D^{*+} \to D^0\pi^+$ and (h–j) $D^{*0} \to D^0\pi^0$. Events with ΔE within 2.5σ of the Gaussian mean value are shown. The top curve is the sum of $P_{\rm sig}$ and the $P_{\rm bgd}$ and the bottom curve is the latter. We note that the plots in (b, c, e, f) had difficulties with fit convergence; see text.

TABLE II. Main results of this paper: B-meson branching fractions for the ten modes. Also given are the values of χ^2, the degrees of freedom (DOF), and the χ^2 probabilities for the averaging of the results from Table I. The measurements are consistent with the previous results.

N-body	B-meson decay mode	$\mathcal{B} \pm \sigma_{\rm stat} \pm \sigma_{\rm syst}$ (10^{-4})	χ^2/DOF	Prob(χ^2) (%)	$\mathcal{B}$ from Refs. [2,5] (10^{-4})	$\mathcal{B}$ from Ref. [4] (10^{-4})
Three-body	$\bar{B}^0 \to D^0 p\bar{p}$	$1.02 \pm 0.04 \pm 0.06$	4.3/2	12	$1.18 \pm 0.15 \pm 0.16$ [5]	$1.13 \pm 0.06 \pm 0.08$
//	$\bar{B}^0 \to D^{*0} p\bar{p}$	$0.97 \pm 0.07 \pm 0.09$	4.1/2	13	$1.20 \pm {}^{0.33}_{0.29} \pm 0.21$ [5]	$1.01 \pm 0.10 \pm 0.09$
Four-body	$\bar{B}^0 \to D^+ p\bar{p}\pi^-$	$3.32 \pm 0.10 \pm 0.29$	...	...	...	$3.38 \pm 0.14 \pm 0.29$
//	$\bar{B}^0 \to D^{*+} p\bar{p}\pi^-$	$4.55 \pm 0.16 \pm 0.39$	1.2/2	54	$6.5 \pm {}^{1.3}_{1.2} \pm 1.0$ [2]	$4.81 \pm 0.22 \pm 0.44$
//	$B^- \to D^0 p\bar{p}\pi^-$	$3.72 \pm 0.11 \pm 0.25$	3.4/2	19	...	...
//	$B^- \to D^{*0} p\bar{p}\pi^-$	$3.73 \pm 0.17 \pm 0.27$	0.5/2	79	...	...
Five-body	$\bar{B}^0 \to D^0 p\bar{p}\pi^-\pi^+$	$2.99 \pm 0.21 \pm 0.45$	0.3/2	85	...	...
//	$\bar{B}^0 \to D^{*0} p\bar{p}\pi^-\pi^+$	$1.91 \pm 0.36 \pm 0.29$	0.5/2	78	...	...
//	$B^- \to D^+ p\bar{p}\pi^-\pi^-$	$1.66 \pm 0.13 \pm 0.27$	...	...	...	...
//	$B^- \to D^{*+} p\bar{p}\pi^-\pi^-$	$1.86 \pm 0.16 \pm 0.19$	0.2/2	91	...	...

TABLE III. Ratios of B-meson branching fractions of the modes related by $D \leftrightarrow D^*$, $D^{(*)0} \leftrightarrow D^{(*)+}$, and the addition of π. The uncertainties are statistical.

Ratio of the modes	$R \pm \sigma_R$
Related by spin of charm meson	
$\mathcal{B}(\bar{B}^0 \to D^{*0} p\bar{p})/\mathcal{B}(\bar{B}^0 \to D^0 p\bar{p})$	0.95 ± 0.08
$\mathcal{B}(\bar{B}^0 \to D^{*+} p\bar{p}\pi^-)/\mathcal{B}(\bar{B}^0 \to D^+ p\bar{p}\pi^-)$	1.37 ± 0.06
$\mathcal{B}(B^- \to D^{*0} p\bar{p}\pi^-)/\mathcal{B}(B^- \to D^0 p\bar{p}\pi^-)$	1.00 ± 0.05
$\mathcal{B}(\bar{B}^0 \to D^{*0} p\bar{p}\pi^-\pi^+)/\mathcal{B}(\bar{B}^0 \to D^0 p\bar{p}\pi^-\pi^+)$	0.64 ± 0.13
$\mathcal{B}(B^- \to D^{*+} p\bar{p}\pi^-\pi^-)/\mathcal{B}(B^- \to D^+ p\bar{p}\pi^-\pi^-)$	1.12 ± 0.13
Related by charge of charm meson	
$\mathcal{B}(B^- \to D^0 p\bar{p}\pi^-)/\mathcal{B}(\bar{B}^0 \to D^+ p\bar{p}\pi^-)$	1.12 ± 0.05
$\mathcal{B}(B^- \to D^{*0} p\bar{p}\pi^-)/\mathcal{B}(\bar{B}^0 \to D^{*+} p\bar{p}\pi^-)$	0.82 ± 0.05
$\mathcal{B}(\bar{B}^0 \to D^0 p\bar{p}\pi^-\pi^+)/\mathcal{B}(B^- \to D^+ p\bar{p}\pi^-\pi^-)$	1.80 ± 0.19
$\mathcal{B}(\bar{B}^0 \to D^{*0} p\bar{p}\pi^-\pi^+)/\mathcal{B}(B^- \to D^{*+} p\bar{p}\pi^-\pi^-)$	1.03 ± 0.21
Related by addition of pion to three-body modes	
$\mathcal{B}(B^- \to D^{*0} p\bar{p}\pi^-)/\mathcal{B}(\bar{B}^0 \to D^{*0} p\bar{p})$	3.84 ± 0.33
$\mathcal{B}(B^- \to D^0 p\bar{p}\pi^-)/\mathcal{B}(\bar{B}^0 \to D^0 p\bar{p})$	3.64 ± 0.18
Related by addition of pion to four-body modes	
$\mathcal{B}(B^- \to D^+ p\bar{p}\pi^-\pi^-)/\mathcal{B}(\bar{B}^0 \to D^+ p\bar{p}\pi^-)$	0.50 ± 0.04
$\mathcal{B}(B^- \to D^{*+} p\bar{p}\pi^-\pi^-)/\mathcal{B}(\bar{B}^0 \to D^{*+} p\bar{p}\pi^-)$	0.41 ± 0.04
$\mathcal{B}(\bar{B}^0 \to D^0 p\bar{p}\pi^-\pi^+)/\mathcal{B}(\bar{B}^0 \to D^0 p\bar{p}\pi^-)$	0.80 ± 0.06
$\mathcal{B}(\bar{B}^0 \to D^{*0} p\bar{p}\pi^-\pi^+)/\mathcal{B}(\bar{B}^0 \to D^{*0} p\bar{p}\pi^-)$	0.51 ± 0.10

A. Sources

The sources of systematic uncertainties, which are listed in Table IV, can be organized as follows:

(i) Counting of the number of $B\bar{B}$ pairs,
(ii–iv) Assumed branching fractions,
(v–xi) Reconstruction efficiencies,
(xii–xv) Fit functions and its parameters, and
(xvi–xvii) Backgrounds peaking in $M_{\rm ES}$ or ΔE.

These contributions are described below.

(i) The number of $B\bar{B}$ pairs used in the analysis is the difference of the observed number of hadronic events and the expected contribution from continuum events. The latter is estimated using a separate data sample taken 40 MeV below the $\Upsilon(4S)$ peak. The uncertainty of 1.1% is mostly due to the difference in the detection efficiencies for hadronic events in the data and the MC samples.

(ii) The $\Upsilon(4S)$ branching fraction is assumed to be equal for $B^0\bar{B}^0$ and B^+B^-. The uncertainty of 3.2% is the difference of $1/2$ and the PDG value [6].

(iii) The D- and D^*-meson branching fractions assume the PDG values [6]. The uncertainties of 1.3%, 3.7%, 2.5%, and 2.3% are the PDG uncertainties for $D^0 \to K^-\pi^+$, $K^-\pi^+\pi^0$, $K^-\pi^+\pi^-\pi^+$, and $D^+ \to K^-\pi^+\pi^+$, respectively; and 4.7% and 0.7% for $D^{*0} \to D^0\pi^0$ and $D^{*+} \to D^0\pi^+$, respectively.

(iv) The charged track reconstruction efficiency is evaluated using $e^+e^- \to \tau^+\tau^-$ events, where one tau decays leptonically and the other hadronically. The uncertainty of 0.5% is due to the difference between the detection efficiency in the data and the MC samples.

(v) The reconstruction efficiency of low-energy charged pion from $D^{*+} \to D^0\pi^+$ decays is sufficiently difficult, in comparison to other tracks, that item (v) cannot account for its uncertainty. Such a pion is often found using only the silicon vertex tracker because its momentum is relatively low. The momentum dependence of pion identification is evaluated using the helicity angle $\theta_{\rm hel}$ distribution—the angle between the pion direction in the D^{*+} rest frame and the D^{*+} boost direction—because the two quantities are highly correlated. Since the pions are produced symmetrically in $\cos\theta_{\rm hel}$, the observed asymmetry in the distribution is indicative of the momentum dependence of the efficiency. The uncertainty of 3.1% is due to the difference in the momentum dependence in the data and the MC samples.

(vi) The π^0 reconstruction efficiency is evaluated using $\tau^+\tau^-$ events as in item (v) with an uncertainty of 3.0%.

(vii) The signal B-candidate reconstruction efficiency is evaluated using the MC samples. Since these samples use the uniform phase-space decay model while the reported baryonic decay dynamics ([2,4,5,10–15], this paper) are far from uniform, corrections are made in the variables where the strongest variation are seen—in bins of $M^2(p\bar{p})$ vs $M^2(D^{(*)}p)$—using the data and the MC samples. The uncertainties ranging from 0.8% to 9.7% are due to the limited statistics of the samples.

(viii) The particle identification efficiencies for kaons and protons are evaluated using the MC samples, which are then corrected using a data sample rich in these hadrons. The uncertainties ranging from 1.5% to 2.5% are due to the sample statistics associated with the correction procedure. The sample, however, is dominated by the continuum events whose event topology is different from $B\bar{B}$ events. Items (x, xi) account for the differences.

(ix) The kaon and proton identification efficiencies in the $B\bar{B}$ environment are evaluated using a data sample of $D^{*+} \to D^0\pi^+$, $D^0 \to K^-\pi^+$ and $\Lambda \to p\pi^-$ decays, respectively. The uncertainties of 0.5% and 1.0%, respectively, are due to the differences in the event topologies.

(x) A subset of the fit function parameters is fixed when fitting the $M_{\rm ES}$-ΔE distributions in the data sample. Such parameter values are obtained by fitting the MC distributions, and they are assigned an uncertainty from this fit. The effect on the signal yield is evaluated by fitting the data sample with the

TABLE IV. Systematic uncertainty list for B-meson branching fractions. The "D modes" represents $D^0 \to K^-\pi^+$, $K^-\pi^+\pi^0$, and $K^-\pi^+\pi^-\pi^+$; and $D^+ \to K^-\pi^+\pi^+$.

Item	Description	Uncertainty (%)
i	Number of $B\bar{B}$ pairs	1.1
ii	$\mathcal{B}(\Upsilon(4S))$: for $\Upsilon(4S) \to B\bar{B}$	3.2
iii	$\mathcal{B}(D)$: for D modes	1.8, 4.4, 3.2, 3.6
iv	$\mathcal{B}(D^*)$: for $D^* \to D^0\pi^0$, $D^{*+} \to D^0\pi^+$	4.7, 0.7
v	Charged particle reconstruction	0.5
vi	π^+ from $D^{*+} \to D^0\pi^+$	3.1
vii	π^0 reconstruction	3.0
viii	Signal mode decay dynamics	0.8–9.7
ix	Kaon and proton identification using data	1.5–2.5
x	Kaon identification in $B\bar{B}$ event topology	0.5
xi	Proton identification in $B\bar{B}$ event topology	1.0
xii	Fit function parameters: for D modes	1.3, 2.8, 5.7, 3.4
xiii	Signal fit function	0.6
xiv	Background fit function: for D modes	0.8, 4.5, 1.3, 2.0
xv	$M_{\rm ES}$-ΔE correlation	0.4–2.2
xvi	Background peaking in $M_{\rm ES}$ or ΔE for all modes (marked "a" in Table I)	0–5.5 (77–85)
xvii	Background from baryonic B-decay modes	0.5–13.5

parameter value shifted by 1σ. The procedure is repeated for each parameter in the set. The uncertainties of 1.3%, 2.8%, 5.7%, and 3.4% for the modes with $D^0 \to K^-\pi^+$, $K^-\pi^+\pi^0$, $K^-\pi^+\pi^-\pi^+$, $K^-\pi^+\pi^+$, and $D^+ \to K^-\pi^+\pi^+$, respectively, are the quadrature sum of the fractional yield changes.

(xi) The choice of the signal fit function is evaluated using an alternate function, a fourth-order polynomial. The uncertainty of 0.6% is due to the yield difference with respect to the original fit function.

(xii) The choice of the background fit function is evaluated using a more general fit function with the addition of another such component. The uncertainties—0.8%, 4.5%, 1.3%, and 2.0% for the modes with $D^0 \to K^-\pi^+$, $K^-\pi^+\pi^0$, $K^-\pi^+\pi^-\pi^+$, and $D^+ \to K^-\pi^+\pi^+$, respectively—are due to the yield differences with respect to the original fit function.

(xiii) The small correlation between the $M_{\rm ES}$ and ΔE distributions introduces a bias in the signal yield. This effect is quantified by fitting pseudoexperiments. Each experiment contains a background sample whose $M_{\rm ES}$ and ΔE distributions are produced according to $P_{\rm bgd}$, and a signal MC sample from the full detector simulation. The uncertainties ranging from 0.1% to 1.8% are from the deviation of $N_{\rm sig}$ to the mean of the signal-yield distribution.

(xiv) Background events whose distributions peak either at $M_{\rm ES} = 5.28\ {\rm GeV}/c^2$ or $\Delta E = 0$ can alter the signal yield. For the $B^- \to D^{*0}p\bar{p}\pi^-$ measurement, the variation of the normalization of the fit function for the $\bar{B}^0 \to D^{*+}p\bar{p}\pi^-$ contribution

TABLE V. Systematic uncertainties (%) combined for the B modes. For each D mode, two columns are given. The uncorrelated values are given on the left columns and the correlated on the right columns. The right columns exclude items (iii, iv) of Table IV.

B mode/$D \to$	$K^-\pi^+$		$K^-\pi^+\pi^0$		$K^-\pi^+\pi^-\pi^+$		$K^-\pi^+\pi^+$	
	uncorr	corr	uncorr	corr	uncorr	corr	uncorr	corr
$\bar{B}^0 \to D^0p\bar{p}$	2.7	3.5	5.5	6.9	4.7	7.0	...	...
$\bar{B}^0 \to D^{*0}p\bar{p}$	2.2	4.6	8.6	8.6	8.7	7.7	...	...
$\bar{B}^0 \to D^+p\bar{p}\pi^-$	...	...	...	...	...	...	5.7	5.7
$\bar{B}^0 \to D^{*+}p\bar{p}\pi^-$	4.2	6.3	7.6	8.6	9.9	8.9	...	...
$\bar{B}^0 \to D^0p\bar{p}\pi^-\pi^+$	14.5	3.9	81.2	7.0	77.3	7.0	...	...
$\bar{B}^0 \to D^{*0}p\bar{p}\pi^-\pi^+$	13.8	4.9	86.3	8.8	85.4	7.7	...	...
$B^- \to D^0p\bar{p}\pi^-$	4.4	4.2	8.8	7.2	11.6	7.3	...	...
$B^- \to D^{*0}p\bar{p}\pi^-$	6.6	5.2	8.4	8.9	10.5	7.9	...	...
$B^- \to D^+p\bar{p}\pi^-\pi^-$	...	...	...	...	...	...	15.0	5.9
$B^- \to D^{*+}p\bar{p}\pi^-\pi^-$	5.9	6.8	14.9	9.0	19.0	9.2	...	...

within the experimental uncertainties has a negligible effect on the signal yield. For other B decay modes, no such sources are found. However, the $M_{\rm ES}$ distributions for a few cases feature a broad hump with a width around 20 MeV/c^2 spanning nearly half of the signal box. The effect of the presence of such a source is quantified by adding a component $P_{\rm peak}$ to the fit function whose parameters are fixed except for the normalization. Except for four decay chains—those corresponding to Figs. 7(b), 7(c), 7(e), and 7(f)—uncertainties ranging from zero to 5.5% are obtained from the changes in yield when the additional component is included. For the mentioned exceptions, the uncertainties range from 77% to 85%. As a consequence of the large uncertainties, these four modes do not contribute significantly to the final results.

(xv) Background events from baryonic modes without a D meson are evaluated using the data sample. An example case where the final states are identical is $B \to \Lambda_c \bar{p}\pi^0$, $\Lambda_c \to pK^-\pi^+$ and $\bar{B}^0 \to D^0 p\bar{p}$, $D^0 \to K^-\pi^+\pi^0$. For such a source, the $M(D)$ distribution does not peak at the D mass, so the contamination can be quantified by repeating the analysis with the $M(D)$-sideband region. $N_{\rm peak}$ is an additive correction factor for $N_{\rm sig}$ with uncertainties ranging from 0.5% to 13.5% due to the sample statistics.

B. Error matrices

The error matrix, V, spanning the D modes of a given B mode is the sum of the statistical and systematic components $V = V_{\rm stat} + V_{\rm syst}$.

The $V_{\rm stat}$ is diagonal with elements $(\sigma_{{\rm stat},\alpha})^2$ (Table I).

The $V_{\rm syst}$ is the sum of a diagonal part and an off-diagonal part $V_{\rm syst} = V_{\rm unc} + V_{\rm cor}$ (Table V). The $V_{\rm unc}$ is diagonal with $(\sigma_{{\rm unc},\alpha})^2$. The $V_{\rm cor}$ is the sum of a diagonal part with $(\sigma_{{\rm cor},\alpha})^2$ and an off-diagonal part with $\rho_{\alpha\beta}\sigma_{{\rm cor},\alpha}\sigma_{{\rm cor},\beta}$. The correlation coefficient $\rho_{\alpha\beta}$ is between two D^0 modes α and β. The correlations among D^0-meson branching fractions are the PDG values [6]; all others are assumed to be unity.

VI. KINEMATIC DISTRIBUTIONS

This section presents the kinematic distributions [45]. Sections VI A, VI B, and VI C, give the plots for three-, four-, and five-body modes, respectively. Additional discussion is devoted to the $M(p\pi^-)$ feature in Sec. VI D.

We briefly describe the background-subtraction and efficiency-correction methods used to obtain the differential branching fraction plots as a function of two-body invariant mass variables. The differential branching fraction, in bins j of the plotted variable, is the ratio of the number of signal events and the product of the correction factors as given in Eq. (5). The quantity in the numerator is the sum of the background-subtracted

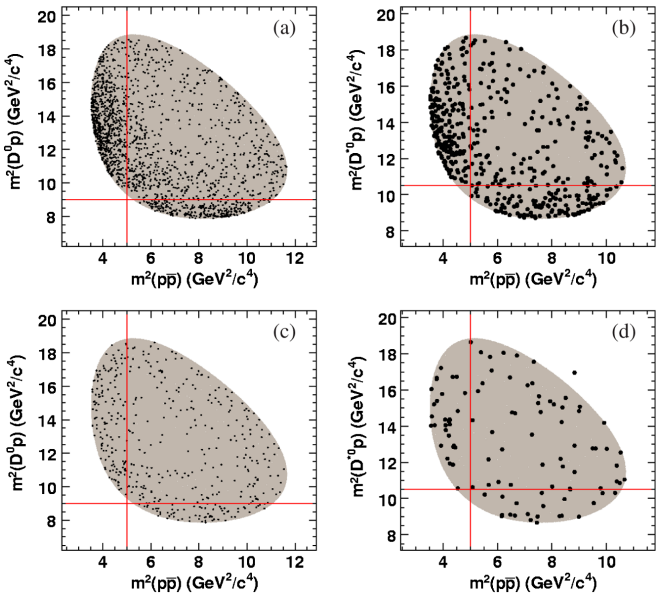

FIG. 8 (color online). Dalitz plots $M^2(p\bar{p})$ vs $M^2(D^{(*)0}p)$ for the three-body modes. Plots in the first column (a, c) correspond to $\bar{B}^0 \to D^0 p\bar{p}$; the second column (b, d) $\bar{B}^0 \to D^{*0} p\bar{p}$. Plots in the first row (a, b) are the events in the $M_{\rm ES} - \Delta E$ signal box; the second row (c, d) the events in the $M_{\rm ES}$-sideband region normalized to the amount of background present in the respective plots in the first row. In the first row, near-threshold enhancements are seen compared to the respective sideband plots in the second row. The lines drawn at $M^2(p\bar{p}) = 5$, $M^2(D^0p) = 9$, and $M^2(D^{*0}p) = 10.5$ GeV$^2/c^4$ are visual aides to show that the enhancements are mostly non-overlapping. The events are contained in the shaded contour representing the allowed kinematic region except for one outlier in (d), which failed the fit. The points are made larger for the plots in the second column for better visibility.

event weights for events in bin j; the formulae are given below. The efficiency-correction part of the denominator is found for bin j and is applied to each event weight.

The S-plot method is used [46] to find the event weight,

$$W(y_i) = \frac{\rho_{\mathrm{sig,sig}} P_{\mathrm{sig}}(y_i) + \rho_{\mathrm{sig,bgd}} P_{\mathrm{bgd}}(y_i)}{N_{\mathrm{sig}} P_{\mathrm{sig}}(y_i) + N_{\mathrm{bgd}} P_{\mathrm{bgd}}(y_i)}, \quad (6)$$

where the y_i is the pair of M_{ES} and ΔE values for the candidate in the ith event; the fit functions P_α were defined in Eq. (4). In general, the weight W is approximately 0 for a background event and 1 for a signal event. The $\rho_{\mathrm{sig,bgd}}$ quantifies the correlation between the signal and the background yields,

$$(\rho_{\lambda,\lambda'})^{-1} = \sum_{i=1}^{N} \frac{P_\lambda(y_i) P_{\lambda'}(y_i)}{(N_{\mathrm{sig}} P_{\mathrm{sig}}(y_i) + N_{\mathrm{bgd}} P_{\mathrm{bgd}}(y_i))^2}. \quad (7)$$

A. Three-body modes $B \to D^{(*)} p\bar{p}$

For the three-body modes, plots are given for Dalitz variables and two-body invariant masses.

The Dalitz plots of $M^2(D^{(*)0}p)$ vs $M^2(p\bar{p})$ for the events in the M_{ES}-ΔE signal box are given [Fig. 8(a) and 8(b)]. The allowed kinematic region is the shaded contour.

The background events present in Figs. 8(a) and 8(b) are represented by Figs. 8(c) and 8(d), respectively. The latter plots show the events in the M_{ES}-sideband regions with their normalizations determined from the background yield in the signal box.

The two-body invariant mass plots are given in Fig. 9. Differential branching fractions are plotted as a function of $M(D^{(*)0}p)$ and $M(p\bar{p})$ for events in different regions of the complementary variable. The two low-mass enhancements near threshold values in $M(D^{(*)0}p)$ and $M(p\bar{p})$ correspond to the dense regions in the Dalitz plots.

The observed $M(D^{(*)0}p)$ enhancements below 3 GeV/c^2 for the kinematic region of $M(p\bar{p}) > 2.24$ GeV/c^2 [Figs. 9(a) and 9(e)] are unlikely to have significant contributions from decays of known intermediate states $\Lambda_c(2880, 2940)^+$ [47] because their widths are too narrow (5.8 and 17 MeV/c^2, respectively) with respect to the broad 200 MeV/c^2 structure.

The observed $M(p\bar{p})$ enhancements near 3.1 GeV/c^2 for the kinematic region for low values of $M(D^{(*)0}p)$—below 3 (3.24) GeV/c^2 for the mode with $D^0(D^{*0})$—[Figs. 9(d) and 9(h)] are unlikely to be from J/ψ decays because of its narrow width (93 keV/c^2) with respect to the broad 100–200 MeV/c^2 structure as well as the current experimental limit on $\bar{B}^0 \to D^0 J/\psi$ production [48].

In general, we observe a strong similarity between the shapes of the corresponding distributions for $\bar{B}^0 \to D^0 p\bar{p}$ and $\bar{B}^0 \to D^{*0} p\bar{p}$.

B. Four-body modes $B \to D^{(*)} p\bar{p}\pi$

For the four-body modes, plots are given for two-body invariant masses in Fig. 10. Differential branching fractions are plotted as a function of $M(p\bar{p})$, $M(D^{(*)}p)$, $M(D^{(*)}\bar{p})$, and $M(p\pi^-)$.

The two-body invariant-mass distributions show a number of features. The $M(p\bar{p})$ distributions show a threshold enhancement with respect to the expectations from the uniform phase-space decay model [Figs. 10(a), 10(e), 10(i), and 10(m)]. The $M(D^{(*)}\bar{p})$ distributions show no indication of a penta-quark resonance at 3.1 GeV/c^2 [49] [Figs. 10(b), 10(f), 10(j), and 10(n)]. The $M(D^{(*)}p)$ distribution in $\bar{B}^0 \to D^0 p\bar{p}\pi^-$ [Fig. 10(k)] shows a threshold enhancement. However, it is unlikely to be from

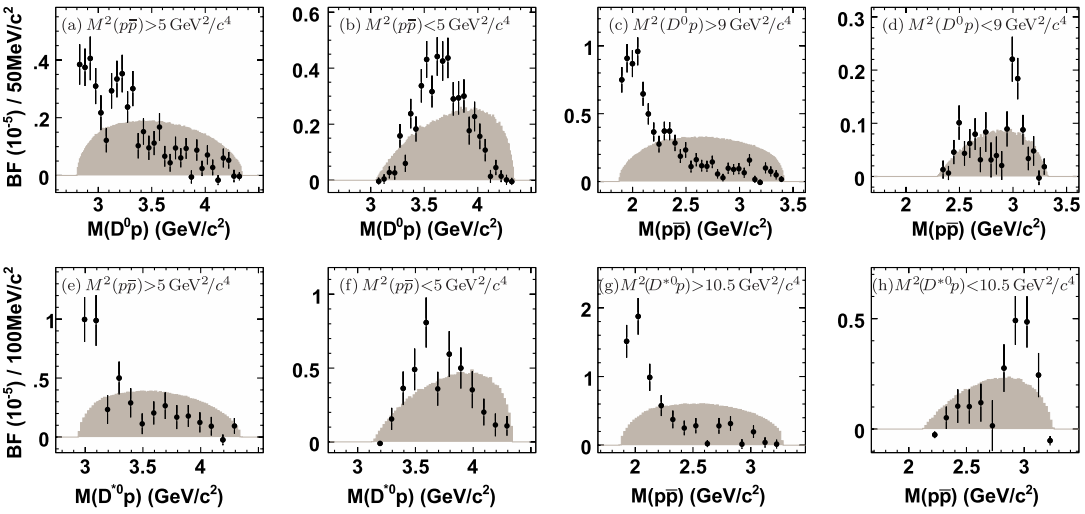

FIG. 9 (color online). Differential branching fraction plots for the three-body B-meson modes: (a–d) $\bar{B}^0 \to D^0 p\bar{p}$ and (e–h) $\bar{B}^0 \to D^{*0} p\bar{p}$. The captions give the various phase-space regions. The shaded region represents the uniform phase-space model with its area normalized to the data. The bin width for each row of plots is given on the leftmost plot.

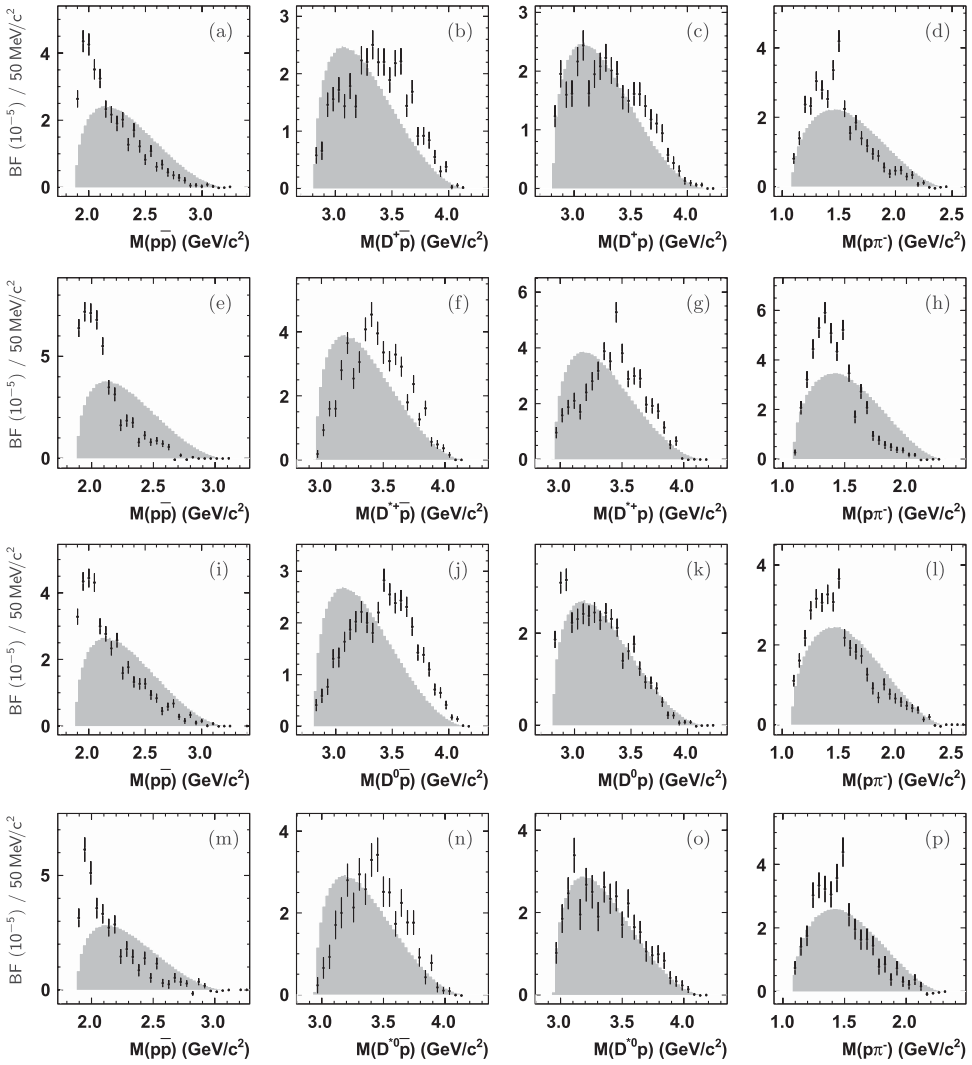

FIG. 10. Differential branching fraction plots as functions of $M(p\bar{p})$, $M(D^{(*)}p)$, $M(D^{(*)}\bar{p})$, and $M(p\pi^-)$ for the four-body B-meson modes: (a, b, c, d) $\bar{B}^0 \to D^+ p\bar{p}\pi^-$, (e, f, g, h) $\bar{B}^0 \to D^{*+} p\bar{p}\pi^-$, (i, j, k, l) $B^- \to D^0 p\bar{p}\pi^-$, and (m, n, o, p) $B^- \to D^{*0} p\bar{p}\pi^-$, respectively. The shaded region represents the uniform phase-space model normalized to the data. The possible presence of a narrow peak near 1.5 GeV/c^2 in plots in (d, h, j, p) are shown in detail in Figs. 12(a)–12(d), respectively, and discussed in Sec. VI D. The bin width for each row of plots is given on the left.

$\Lambda_c(2880, 2940)^+$ decays, which have narrow widths, as was discussed in the previous section. The distributions in the other modes show no such features [Figs. 10(c), 10(g), and 10(o)]. The $M(p\pi^-)$ distribution in one of the modes [Fig. 10(d)] shows a narrow structure near 1.5 GeV/c^2, but it is less prominent in the distributions of the other modes [Figs. 10(h), 10(l), and 10(p)].

The peak near 1.5 GeV/c^2 does not correspond to a known state. The peak is discussed in detail in Sec. VI D.

C. Five-body modes $B \to D^{(*)} p\bar{p}\pi\pi$

For the five-body modes, plots are given for two-body invariant masses in Fig. 11. Branching fractions are plotted as a function of $M(p\bar{p})$, $M(D^{(*)}p)$, $M(D^{(*)}\bar{p})$, and $M(p\pi^-)$.

In contrast to the distributions for the three- and four-body modes, the five-body distributions are generally more consistent with the expectations from the uniform phase-space decay model.

A notable absence, again, is the signal of a pentaquark resonance at 3.1 GeV/c^2 [49] [Figs. 11(b), 11(f), 11(j), and 11(n)].

D. Narrow $M(p\pi^-)$ peak at 1.5 GeV/c^2

The narrow peak in the $M(p\pi^-)$ [50] distribution at 1.5 GeV/c^2, which we refer to as X, is discussed in this section.

The opposite-sign $M(p\pi^-)$ distributions corresponding to Figs. 10(d), 10(h), 10(l), and 10(p) are shown in more detail in Fig. 12. In the detailed plots, the x-axis bin width

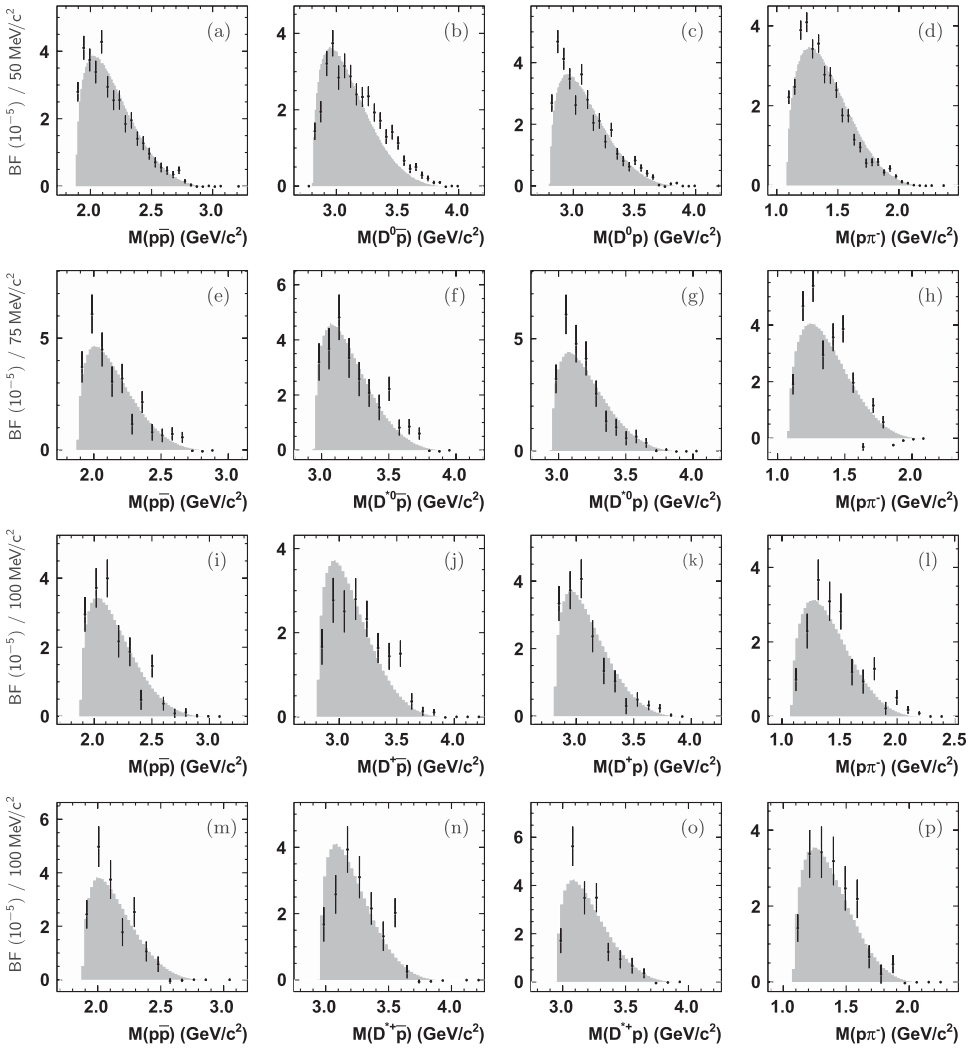

FIG. 11. Differential branching fraction plots as functions of $M(p\bar{p})$, $M(D^{(*)}p)$, $M(D^{(*)}\bar{p})$, and $M(p\pi^-)$ for five-body B-meson modes: (a, b, c, d) $\bar{B}^0 \to D^0 p\bar{p}\pi^-\pi^+$, (e, f, g, h) $\bar{B}^0 \to D^{*0} p\bar{p}\pi^-\pi^+$, (i, j, k, l) $B^- \to D^+ p\bar{p}\pi^-\pi^-$, and (m, n, o, p) $B^- \to D^{*+} p\bar{p}\pi^-\pi^-$, respectively. The shaded region represents the uniform phase-space model normalized to the data. Each B-meson candidate for the plots in (d, h) contributes two entries for both $p\pi^-$ and $\bar{p}\pi^+$ combinations, so they are scaled accordingly. The bin width for each row of plots is given on the left.

is smaller at 10 MeV/c^2 and the y axis is the unweighted-uncorrected number of events. The events from the $M_{\rm ES}$-sideband region is superimposed with its normalization determined from the background yield in the $M_{\rm ES}$-ΔE signal box.

In order to measure the properties of the peak, the fit formalism of Eq. (4) is used. The signal component $P_{\rm sig}$ is assumed to be a Breit-Wigner line shape. The background component $P_{\rm bgd}$ is taken from the same-sign $M(\bar{p}\pi^-)$ distribution. The distribution for the $\bar{B}^0 \to D^+ p\bar{p}\pi^-$ mode is relatively smooth [Fig. 13(a)], and it describes the rise and fall of the opposite-sign distribution well [Fig. 12(a)], whereas the same-sign distributions in the other modes show a more rapidly falling behavior around 1.5 GeV/c^2 [Figs. 13(b)–13(d)].

We note, however, that the use of the shape for $P_{\rm bgd}$ has limitations. Since the formation of the p or $\bar{p}$ is not necessarily symmetric with respect to the π^- in these decays, the same-sign $M(\bar{p}\pi^-)$ combination may not predict the true shape for the nonresonant component in the opposite-sign $M(p\pi^-)$ distribution. As a consequence, we cannot precisely quantify the systematic uncertainty associated with the lack of knowledge of the true background shape.

For the two neutral B modes, the fits of the opposite-sign distributions describe the entire kinematic range well [Figs. 12(a) and 12(b)). We note a small excess of events above 1.65 GeV/c^2 with respect to $P_{\rm bgd}$, but no peak component is included in the fit at this mass. The fitted X mass is 1494.4 ± 4.1 MeV/c^2 and 1500.8 ± 4.4 MeV/c^2,

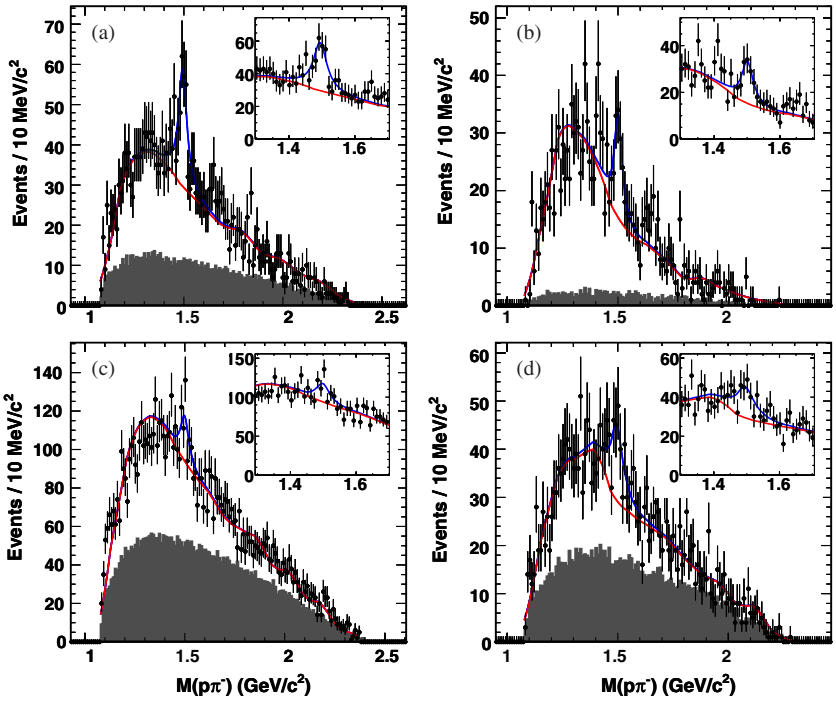

FIG. 12 (color online). Fits of the opposite-sign $M(p\pi^-)$ distribution for (a) $\bar{B}^0 \to D^+ p\bar{p}\pi^-$, (b) $\bar{B}^0 \to D^{*+} p\bar{p}\pi^-$, (c) $B^- \to D^0 p\bar{p}\pi^-$, and (d) $B^- \to D^{*0} p\bar{p}\pi^-$ for events in the signal box of $M_{\rm ES}$-ΔE. The top curve is the sum of $P_{\rm sig}$ and $P_{\rm bgd}$ while the bottom curve is $P_{\rm bgd}$. The $P_{\rm bgd}$ is from the corresponding plot in Fig. 13. The shaded histograms are scaled $M_{\rm ES}$ sidebands. A small inset plot is a close-up of the region around 1.5 GeV/c^2; its bin width is the same as in the larger plot.

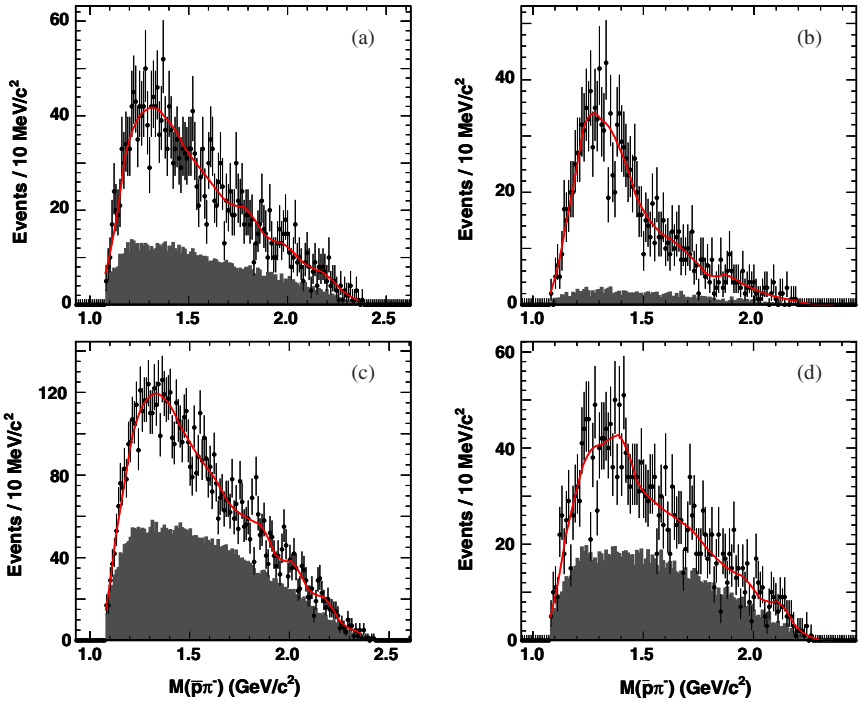

FIG. 13 (color online). Fits of the same-sign $M(\bar{p}\pi^-)$ distribution for (a) $\bar{B}^0 \to D^+ p\bar{p}\pi^-$, (b) $\bar{B}^0 \to D^{*+} p\bar{p}\pi^-$, (c) $B^- \to D^0 p\bar{p}\pi^-$, and (d) $B^- \to D^{*0} p\bar{p}\pi^-$ for events in the signal box of $M_{\rm ES}$-ΔE. The curve is the smoothed histogram that is used in the corresponding plot in Fig. 12 as $P_{\rm bgd}$. The shaded histograms are scaled $M_{\rm ES}$ sidebands.

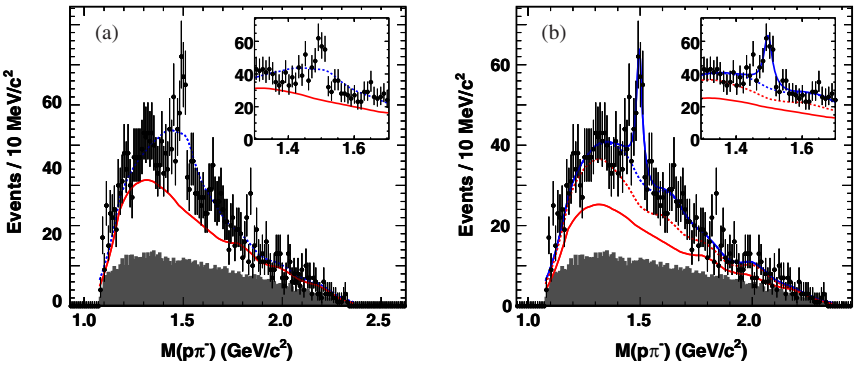

FIG. 14 (color online). Alternate fits of the opposite-sign $M(p\pi^-)$ distribution for $\bar{B}^0 \to D^+ p\bar{p}\pi^-$ with (a) various N^* resonances and (b) an additional $P_{\rm bgd}$ obtained from the $\bar{B}^0 \to D^{*+} p\bar{p}\pi^-$ sample. The shaded histograms are the scaled $M_{\rm ES} - \Delta E$ sidebands. A small inset plot is a close-up of the region around 1.5 GeV/c^2; its bin width is the same as the larger plot.

where the uncertainties are statistical, for $\bar{B}^0 \to D^{*+} p\bar{p}\pi^-$ and $\bar{B}^0 \to D^+ p\bar{p}\pi^-$, respectively. We measure the full widths to be 51 ± 18 MeV/c^2 and 43 ± 17 MeV/c^2, respectively. The widths are significantly wider than detector resolution, which is less than 4 MeV/c^2 for a simulated $X \to p\pi^-$ decay with a mass of 1.5 GeV/c^2 and negligible width.

In contrast to the neutral B modes, the opposite-sign distributions for the two charged B modes exhibit a less peaking behavior at 1.5 GeV/c^2. As a result, the parameter for the width in the $B^- \to D^0 p\bar{p}\pi^-$ mode is fixed to the value found in the $\bar{B}^0 \to D^+ p\bar{p}\pi^-$ mode; the results of this fit are not used in the average.

The known nucleon resonances N^* with the masses 1440, 1520, 1535, and 1650 MeV/c^2 are used in an attempt to describe the X. The distribution is fit with the N^* fit function components each parameterized as a Breit-Wigner line shape. The normalization for each component is allowed to vary independently. However, the fit does not describe the peak because the X is much narrower than any of the N^* resonances [Fig. 14(a)].

The overall significance of the X is difficult to measure, due to our lack of knowledge of the true background shape, as discussed earlier, as well as further statistical issues. We caution that the X analysis is not blind, the parameters are not chosen *a priori*, and the distribution under the no-X hypothesis may be only approximately normal. Furthermore, even under the normal assumption, the presence of the mass and width nuisance parameters under the alternative hypothesis means that the distributions of the S statistic is not likely to be pure χ^2.

We provide a measure of the statistical significance $S = \sqrt{2(\ln L_1 - \ln L_0)}$ of the X in the two neutral B modes, where L_1 is the likelihood value with $P_{\rm sig}$ and L_0 is without $P_{\rm sig}$. The value is $S = 8.6$ for $\bar{B}^0 \to D^+ p\bar{p}\pi^-$ and $S = 6.9$ for $\bar{B}^0 \to D^{*+} p\bar{p}\pi^-$.

The systematic uncertainties are mainly due to the $P_{\rm bgd}$. We fit using an alternate fit function by adding a component derived from the same-sign distribution of a different mode [Fig. 14(b)]. The result is a mass shift of 0.8 MeV/c^2 and a full width change of 4 MeV/c^2. An additional contribution of 0.5 MeV/c^2 is added for the mass measurement due to the absolute uncertainty of the magnetic field and the amount of detector material [51].

In summary, the unknown structure X can be characterized by a Breit-Wigner line shape:

$$M(X) = 1497.4 \pm 3.0 \pm 0.9 \text{ MeV}/c^2$$
$$\Gamma(X) = 47 \pm 12 \pm 4 \text{ MeV}/c^2, \quad (8)$$

where the uncertainties are statistical and systematic, respectively.

VII. CONCLUSIONS

We have presented a study of ten baryonic B-meson decay modes of the form $B \to D^{(*)} p\bar{p}(\pi)(\pi)$ using a data sample of 455×10^6 $B\bar{B}$ pairs. Significant signals are observed (Table I). Six of the modes—$B^- \to D^0 p\bar{p}\pi^-$, $B^- \to D^{*0} p\bar{p}\pi^-$, $\bar{B}^0 \to D^0 p\bar{p}\pi^-\pi^+$, $\bar{B}^0 \to D^{*0} p\bar{p}\pi^-\pi^+$, $B^- \to D^+ p\bar{p}\pi^-\pi^-$, and $B^- \to D^{*+} p\bar{p}\pi^-\pi^-$—are observed for the first time [Figs. 6(e)–6(j), 7(a), 7(d), and 7(g)–7(j), respectively).

The B-meson branching fraction measurements range from 0.97×10^{-4} to 4.55×10^{-4} with the hierarchy $\mathcal{B}_{\text{3-body}} < \mathcal{B}_{\text{5-body}} < \mathcal{B}_{\text{4-body}}$ (Table II). These results supersede the previous *BaBar* publication of $\bar{B}^0 \to D^0 p\bar{p}$, $D^{*0} p\bar{p}$, $D^+ p\bar{p}\pi^-$, and $D^{*+} p\bar{p}\pi^-$ [4]. The branching fractions related by changes in the charge or the spin of the D meson are found to be similar (Table III).

The kinematic distributions show a number of notable features. For the three-body modes, threshold enhancements are present in $M(p\bar{p})$ and $M(D^{(*)0}p)$ (Figs. 8 and 9). For the four-body modes, a threshold enhancement is observed in $M(p\bar{p})$ and a narrow peak is seen in $M(p\pi^-)$ (Fig. 10). For the five-body modes, in contrast to the other modes, the distributions are similar to the expectations from the uniform phase-space decay model (Fig. 11).

The $M(p\pi^-)$ distributions in the neutral B-meson decay mode show the most prominent peak near 1.5 GeV/c^2. We obtained a mass of $1497.4 \pm 3.0 \pm 0.9$ MeV/c^2 and a full width of $47 \pm 12 \pm 4$ MeV/c^2, where the first uncertainties are statistical and the second are systematic, respectively, (Figs. 12–14). Determining the significance and interpreting the origin of the peak are complicated by the fact that the background fit function is parameterized by the distribution from the same-sign charge combinations $\bar{p}\pi^-$, a procedure which may not provide the true background shape.

Despite the relatively small branching fractions for these modes of order 10^{-4}, with product branching fractions of order 10^{-5} to 10^{-6} (including the D and D^* modes), the large size of the *BaBar* data sample allowed us to observe signals containing hundreds of events in many of the modes. We are, therefore, able to probe their kinematic distributions that reflect the complex dynamics of the multibody final states.

ACKNOWLEDGMENTS

We are grateful for the extraordinary contributions of our PEP-II colleagues in achieving the excellent luminosity and machine conditions that have made this work possible. The success of this project also relies critically on the expertise and dedication of the computing organizations that support *BaBar*. The collaborating institutions wish to thank SLAC for its support and the kind hospitality extended to them. This work is supported by the US Department of Energy and National Science Foundation, the Natural Sciences and Engineering Research Council (Canada), the Commissariat à l'Energie Atomique and Institut National de Physique Nucléaire et de Physique des Particules (France), the Bundesministerium für Bildung und Forschung and Deutsche Forschungsgemeinschaft (Germany), the Istituto Nazionale di Fisica Nucleare (Italy), the Foundation for Fundamental Research on Matter (The Netherlands), the Research Council of Norway, the Ministry of Education and Science of the Russian Federation, Ministerio de Ciencia e Innovación (Spain), and the Science and Technology Facilities Council (United Kingdom). Individuals have received support from the Marie-Curie IEF program (European Union), the A. P. Sloan Foundation (USA) and the Binational Science Foundation (USA-Israel).

[1] X. Fu *et al.* (CLEO Collaboration), Phys. Rev. Lett. **79**, 3125 (1997).
[2] S. Anderson *et al.* (CLEO Collaboration), Phys. Rev. Lett. **86**, 2732 (2001).
[3] I. Dunietz, Phys. Rev. D **58**, 094010 (1998).
[4] B. Aubert *et al.* (*BaBar* Collaboration), Phys. Rev. D **74**, 051101 (2006).
[5] K. Abe *et al.* (Belle Collaboration), Phys. Rev. Lett. **89**, 151802 (2002).
[6] C. Amsler *et al.* (Particle Data Group), Phys. Lett. B **667**, 1 (2008).
[7] B. Aubert *et al.* (*BaBar* Collaboration), Phys. Rev. D **78**, 112003 (2008).
[8] We do not include $\bar{B}^- \to D^{(*)-} p\bar{p}$ in the list because they are beyond our sensitivity due to the λ^2 suppression with respect to $\bar{B}^0 \to D^{(*)0} p\bar{p}$. For the quantity λ^2, see L. Wolfenstein, Phys. Rev. Lett. **51**, 1945 (1983).
[9] We use the convention that charge conjugation of particles and their decays is implied unless otherwise specified.
[10] Y. J. Lee *et al.* (Belle Collaboration), Phys. Rev. Lett. **93**, 211801 (2004).
[11] M. Z. Wang *et al.* (Belle Collaboration), Phys. Rev. D **76**, 052004 (2007).
[12] T. Medvedeva *et al.* (Belle Collaboration), Phys. Rev. D **76**, 051102 (2007).
[13] J. T. Wei *et al.* (Belle Collaboration), Phys. Lett. B **659**, 80 (2008).
[14] J. H. Chen *et al.* (Belle Collaboration), Phys. Rev. Lett. **100**, 251801 (2008).
[15] B. Aubert *et al.* (*BaBar* Collaboration), Phys. Rev. D **72**, 051101 (2005); **76**, 092004 (2007).
[16] W. S. Hou and A. Soni, Phys. Rev. Lett. **86**, 4247 (2001).
[17] C. K. Chua, W. S. Hou, and S. Y. Tsai, Phys. Rev. D **65**, 034003 (2002); **66**, 054004 (2002); Phys. Lett. B **544**, 139 (2002).
[18] H. Y. Cheng and K. C. Yang, Phys. Rev. D **65**, 054028 (2002); **65**, 099901(E) (2002); **66**, 014020 (2002); **66**, 094009 (2002); **67**, 034008 (2003); Phys. Lett. B **533**, 271 (2002); **633**, 533 (2006).
[19] I. I. Bigi, Eur. Phys. J. C **24**, 271 (2002).
[20] C. H. Chang and W. S. Hou, Eur. Phys. J. C **23**, 691 (2002).
[21] H. Y. Cheng and K. C. Yang, Phys. Rev. D **66**, 014020 (2002); **65**, 054028 (2002); **67**, 034008 (2003).
[22] Z. Luo and J. L. Rosner, Phys. Rev. D**67**, 094017 (2003).
[23] H. Y. Cheng, J. Korean Phys. Soc. **45**, S245 (2004); Int. J. Mod. Phys. A **21**, 4209 (2006); Nucl. Phys. B, Proc. Suppl. **163**, 68 (2007).
[24] Y. K. Hsiao, Int. J. Mod. Phys. A **24**, 3638 (2009).
[25] M. Suzuki, J. Phys. G **31**, 755 (2005); **34**, 283 (2007).
[26] T. M. Hong, Ph.D. thesis, University of California, Santa Barbara, SLAC Report No. 940, Works cited (2010) contains a more comprehensive list of the literature.
[27] J. L. Rosner, Phys. Rev. Lett. **21**, 950 (1968); Phys. Rev. D **68**, 014004 (2003); **69**, 094014 (2004); private communications.
[28] A. Datta and P. J. O'Donnell, Phys. Lett. B **567**, 273 (2003).

[29] B. Kerbikov, A. Stavinsky, and V. Fedotov, Phys. Rev. C **69**, 055205 (2004).
[30] C. H. Chang and H. R. Pang, Commun. Theor. Phys. **43**, 275 (2005).
[31] B. Aubert *et al.* (*BaBar* Collaboration), Nucl. Instrum. Methods Phys. Res., Sect. A **479**, 1 (2002).
[32] D. J. Lange, Nucl. Instrum. Methods Phys. Res., Sect. A **462**, 152 (2001).
[33] T. Sjostrand, Comput. Phys. Commun. **82**, 74 (1994).
[34] S. Agostinelli *et al.* (GEANT4 Collaboration), Nucl. Instrum. Methods Phys. Res., Sect. A **506**, 250 (2003).
[35] We follow the notation where $M(D)$ is the invariant mass of the reconstructed daughters of the D-meson candidate.
[36] P. L. Frabetti *et al.* (E687 Collaboration), Phys. Lett. B **331**, 217 (1994).
[37] W. D. Hulsbergen, Nucl. Instrum. Methods Phys. Res., Sect. A **552**, 566 (2005).
[38] B. Aubert *et al.* (*BaBar* Collaboration), Phys. Rev. D **65**, 032001 (2002).
[39] R. J. Barlow, Nucl. Instrum. Methods Phys. Res., Sect. A **297**, 496 (1990).
[40] F. James and M. Roos, Comput. Phys. Commun. **10**, 343 (1975).
[41] W. Verkerke and D. Kirkby, in *Computing in High Energy and Nuclear Physics 2003 Conference Proceedings, La Jolla, California* (unpublished).
[42] R. Brun and F. Rademakers, Nucl. Instrum. Methods Phys. Res., Sect. A **389**, 81 (1997).
[43] M. J. Oreglia, Ph.D. thesis, Stanford University, SLAC Report No. 236, Appendix D (1980); J. E. Gaiser, Ph.D. thesis, Stanford University, Report No. 255, Appendix F (1982).
[44] L. Lyons, D. Gibaut, and P. Clifford, Nucl. Instrum. Methods Phys. Res., Sect. A **270**, 110 (1988).
[45] For Sec. 6, we use a fit strategy where the decay products' momenta are fit while constraining the B-meson candidate's $M(B)$ to the PDG value [6]. In contrast, we do not impose this constraint for the branching-fraction measurements. This strategy ensures that the values of the kinematic variables for all the events lie within the allowed limits.
[46] M. Pivk and F. R. Le Diberder, Nucl. Instrum. Methods Phys. Res., Sect. A **555**, 356 (2005).
[47] B. Aubert *et al.* (*BaBar* Collaboration), Phys. Rev. Lett. **98**, 012001 (2007).
[48] B. Aubert *et al.* (*BaBar* Collaboration), Phys. Rev. D **71**, 091103 (2005).
[49] A. Aktas *et al.* (H1 Collaboration), Phys. Lett. B **588**, 17 (2004).
[50] We refer to both $p\pi^-$ and $\bar{p}\pi^+$ as opposite sign and to both $\bar{p}\pi^-$ and $p\pi^+$ as same sign.
[51] B. Aubert *et al.* (*BaBar* Collaboration), Phys. Rev. D **72**, 052006 (2005).